8-2012

Atomistic Simulations of Defect Nucleation and Intralayer Fracture in Molybdenum Disulphide During Nanoindentation

James A. Stewart
University of Arkansas, Fayetteville

Atomistic Simulations of Defect Nucleation and Intralayer Fracture in Molybdenum Disulphide (MoS$_2$) During Nanoindentation

Atomistic Simulations of Defect Nucleation and Intralayer Fracture in Molybdenum Disulphide (MoS$_2$) During Nanoindentation

A thesis submitted in partial fulfillment
of the requirements for the degree of
Master of Science in Microelectronics-Photonics

By

James A. Stewart, Jr.
Alfred University
Bachelor of Arts in Physics and Mathematics, 2009

August 2012
University of Arkansas

ABSTRACT

Molybdenum disulphide (MoS_2) is a layered, hexagonal crystal that has a very low coefficient of friction. Due to this low coefficient of friction, MoS_2 has become a well-known solid lubricant and liquid lubricant additive. As such, nanoparticles of MoS_2 have been proposed as an additive to traditional liquid lubricants to provide frictional properties that are sensitive to different temperature and pressure regimes. However, to properly design these MoS_2 nanoparticles to be sensitive to different temperature and pressure regimes, it is necessary to understand the mechanical response of crystalline MoS_2 under mechanical loading. Specifically, the fundamental mechanism associated with the nucleation and interaction of defects as well as intralayer fracture. This thesis addressed the mechanical response of crystalline MoS_2 via contact deformation (nanoindentation) simulations, which is representative of the loading conditions experienced by these nanoparticles during synthesis and application.

There are two main tasks to this thesis. First, a Mo-S interatomic potential (a combination of the reactive empirical bond-order (REBO) interatomic potential and the Lennard-Jones 12-6 interatomic potential) that has been parameterized specifically to investigate the tribological properties of MoS_2 was implemented into the classical molecular simulation package, LAMMPS, and refined to provide improved predictions for the mechanical properties of MoS_2 via molecular statics calculations. Second, using this newly implemented interatomic potential, molecular statics calculations were performed to investigate the mechanical response of MoS_2 via nanoindentation with specific focus on the nucleation of defects. Nanoindentation force - displacement curves were compared to the Hertzian contact theory prediction. It was shown that MoS_2 does not follow the Hertzian prediction due it anisotropic nature. In addition, it was shown

that the initial sudden force drop event in the force - displacement curves corresponds to plastic deformation. It was hypothesized that the mechanism associated with plastic failure of MoS_2 was the occurrence of broken bonds. However, it was proven that this initial plastic yield does not correspond to the occurrence of broken bonds in the MoS_2 lattice; instead, a permanent slip occurred within or between the MoS_2 layers.

This thesis is approved for recommendation
to the Graduate Council

Thesis Director:

_____

Dr. Douglas Spearot

Thesis Committee:

_____

Dr. Jacques Chakhalian

_____

Prof. Kenneth Vickers

The following signatories attest that all software used in this thesis was legally licensed for use by James A. Stewart, Jr. for research purposes and publication.

_____   _____

        James A. Stewart Jr.   Dr. Douglas Spearot

This thesis was submitted by James A. Stewart Jr. to http://www.turnitin.com for plagiarism reviewed by the TurnItIn Company's software. I examined the report on this thesis that was returned by that plagiarism review site and attest that in my opinion the items highlighted by the software are incidental to common usage and are not plagiarized material.

_____   _____

      Prof. Kenneth Vickers   Dr. Douglas Spearot
  Director, MicroEP Graduate Program   Thesis Director

THESIS DUPLICATION RELEASE

I hereby authorize the University of Arkansas Libraries to duplicate this thesis when needed for research and/or scholarship.

Agreed_____

James A. Stewart, Jr.

Refused_____

James A. Stewart, Jr.

ACKNOWLEDGEMENTS

DEDICATION

J.S.

TABLE OF CONTENTS

LIST OF TABLES

LIST OF FIGURES

CHAPTER 1: INTRODUCTION

1.1   Background and Motivation

One of the oldest problems in science and technology that also has huge practical importance is that of friction [1, 2]. The friction created between mating surfaces (i.e., contacting surfaces interacting with each other by a relative sliding motion) is the primary cause of failure and increased degradation in mechanical components such as piston rings, engines, bearings, cutting machines, etc. [3, 4, 5, 6]. Friction requires excess energy to be consumed and the combination of friction and excess energy consumption is highly undesirable because as a result of these two effects there will be accelerated wear of mechanical components and a significant decrease in energy efficiency. An example of these problems in everyday life is the fuel economy of a vehicle and the life expectancy of the vehicle's engine [3, 7]. It has been estimated, in developed countries, that approximately 5% of the gross national product (GNP) is wasted in friction and wear problems [1]. It has also been estimated that a developed country can save 1.0 - 1.4% of its GNP if it incorporates tribological principles into its industries [8]. To achieve a reduction in the friction, wear and energy loss associated with mating surfaces, it is necessary to develop effective and durable low-friction surfaces and lubricants [4, 9].

The study of contacting surfaces that are in relative motion with each other and the related problems of friction and wear is the field of tribology [10]. When studying friction and wear and when developing a lubricant, it is necessary to know within which lubrication regime that the components and lubricants will be operating [11, 12]. There are three lubricating regimes that mechanical components can experience: (i) hydrodynamic lubrication, (ii) elastohydrodynamic lubrication, and (iii) boundary lubrication [12, 13, and 14]. The

hydrodynamic regime occurs when a lubricating film is thick enough to completely separate the mating surfaces and isolate the surface asperities (i.e., the distance between mating surfaces is much larger than the asperity size). Asperities are rough and uneven projections on the surface of a material. In this regime, the frictional properties of the system are controlled by the properties of the lubricant [12, 13]. The elastohydrodynamic (or mixed) regime occurs when the lubricating film is thin enough to allow the distance between the mating surfaces to approach the size of the surfaces asperities. In this regime, localized pressure can change the viscosity of the lubricant and elastically deform the sliding surface. Therefore, the controlling factors to characterize the frictional properties of the system are the lubricant viscosity, the viscosity-pressure coefficient and the elastic coefficient of the solid surface [12, 13]. The final regime, which is also known to be the harshest for components, is the boundary lubrication regime. This regime takes place when the mating surfaces are so close together that the lubricating film is unable to prevent significant surface contact, and only a few monolayers of the lubricant are present. This regime has the following main characteristics. First, the mating surfaces are in physical contact and interact at surface asperity locations. Second, the hydrodynamic lubricating effects of the bulk lubricant do not influence the frictional properties. Third, the frictional properties are dominated by the interactions of the asperities and the interaction of the asperities or surfaces with the lubricant [9, 12, 13, 14]. Figure 1.1a shows a schematic of the mating surface positions and the relative positions of the surface asperities in these three lubricating regimes.

Often, the relationship between friction and lubrication is described in a Stribeck curve [12, 13]. A Stribeck curve expresses the coefficient of friction (COF), f, as a function of the lubricant viscosity, η, the sliding velocity, V, and the normal force, F_N [12, 13]. This relationship captures the characteristics of the three lubricating regimes discussed above. Figure 1.1b shows a

schematic representation of a Stribeck curve and the regions of the curve that correspond to and characterize the frictional properties of the three lubricating regimes. Note the region labeling in Figure 1.1 is the reverse of the region order mentioned above.
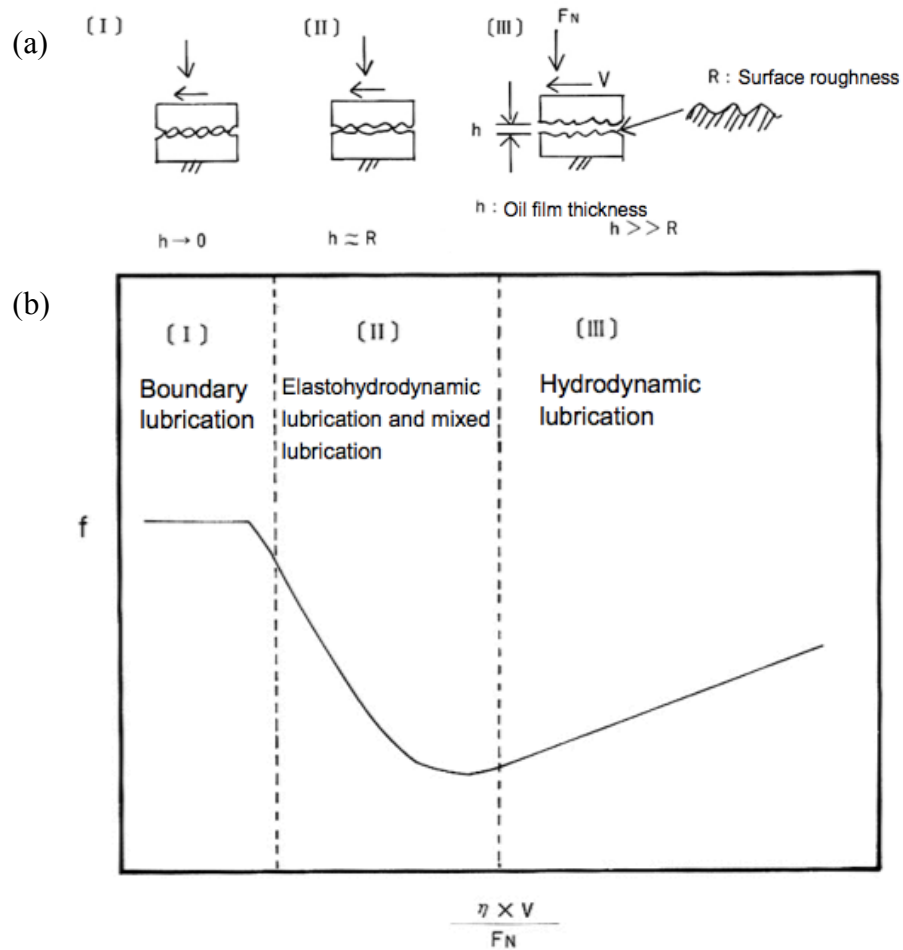
Figure 1.1: (a) A schematic of the relative positions of the mating surfaces in the three lubricating regimes [13] (b) A Stribeck curve illustrating the COF in the three lubricating regimes [13].

Figure 1.1b illustrates that the COF in the boundary lubrication regime is higher during operation relative to the other regimes. This is because of the asperities that exist on the mating surfaces [12, 13, 14]. At low speeds and high loads the lubrication film decreases in thickness.

3

As a result, the asperities are able to come into contact and interact with each other and therefore deform. This is because the lubrication layer ruptures and no longer provides surface protection. This fact permits the boundary lubrication regime to be the harshest regime for mechanical components [12, 13, 14]. Therefore, with this harsh operating condition, the boundary regime will dominate the life cycle of engineering components and materials [15].

The fact that the asperities come into contact with each other means the normal force will not be supported by the entire mating surface (the apparent contact area) or the lubricant. Instead, the force will be supported by the contacting asperities and therefore a much smaller area (the true contact area). The true contact area can be determined by the sum of the contact areas of the surface asperities [9, 13, 14]. A schematic of the boundary lubrication regime in which asperities are in contact and in the presence of a ruptured lubricant is shown in Figure 1.2.
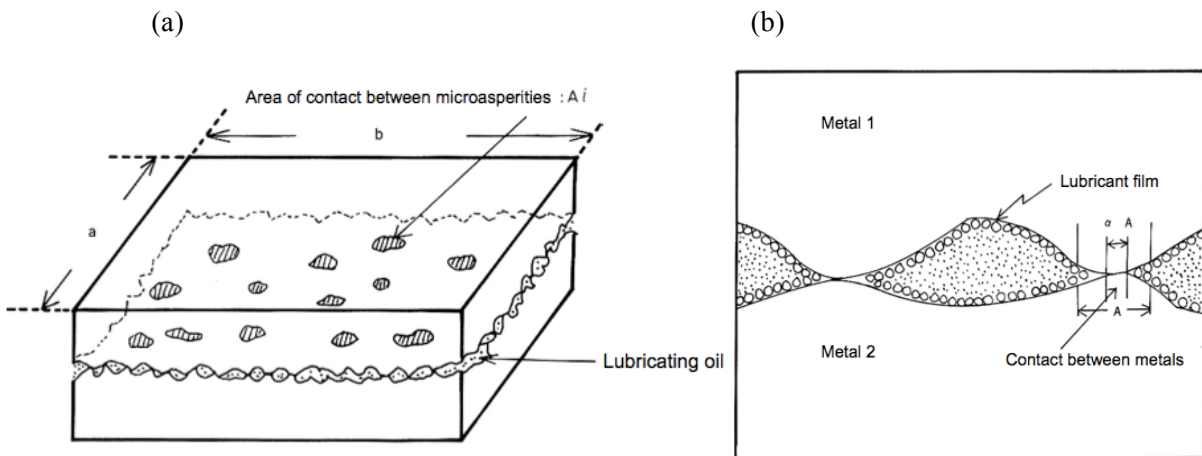
Figure 1.2: (a) Schematic of true surface contact region with contacting asperities [13] (b) Schematic of asperity contact with ruptured lubricant [13].

As a result of the load being supported by the true contact area, an increase in the friction coefficient is accompanied by an increase in pressure and temperature at these contact points [10,

13]. Under these severe conditions (and in general) there are several types of wear that can occur. Adhesive wear is caused by adhesion of the asperities to the contacting surface. Abrasive wear is caused by the removal of material (debris) by the interacting asperities or by particles within the lubricant. Fatigue wear is caused by repeated application of stress to the surface. Chemical wear is caused by chemical reactions between the surfaces and the lubricant [10, 12, 13, 14, 16]. These types of wear can be accelerated by the severe temperatures and pressures introduced in the boundary lubrication regime. These local pressures and temperatures can reach 1-2 GPa and 700 °C respectively [5, 17].

Therefore, it is critical to apply appropriate lubricants such as solid lubricants, oils and greases, oils and greases with special additives (i.e., friction modifiers such as fatty acids, extreme pressure agents, graphite, molybdenum disulphide, etc.) to form lubricating films on components to prevent contact between the surfaces during operation and as a result reduce friction and wear and increase energy efficiency [6, 7, 12, 13]. Figure 1.3 shows a schematic of a Stribeck curve when friction modifiers are present in the lubrication fluid. This Stribeck curve shows a significant reduction of the COF in the boundary lubrication regime as a result of the presence friction modifiers. It is important to note that these lubrication solutions do not work the same way in different environments and operating conditions [18]. A lubricant that works for one system with a specific surface material, temperature and pressure will, in general, not work for another system with a different surface material, temperature and pressure. At the same time, within the same system, what works for one set of operating conditions will not work for another set of operating conditions (i.e., what works at high temperatures and pressures may not work for low temperatures and pressures) [18]. Therefore, it is necessary to be aware of possible operating

conditions and operating environments to be able to choose the most suitable lubricant and/or additive for a given application.
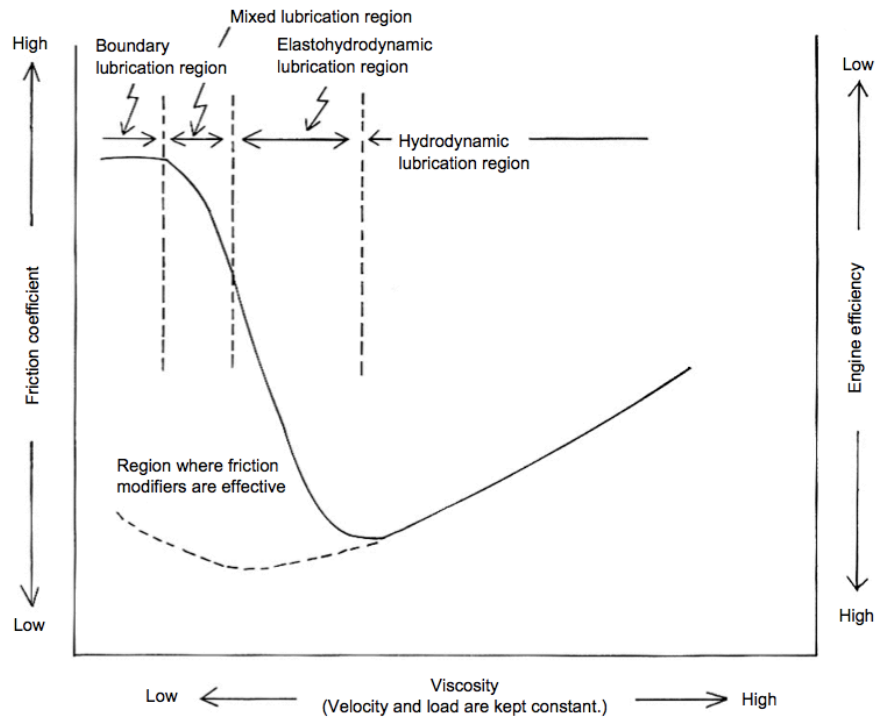
Figure 1.3: A Stribeck curve illustrating the COF in the presence of friction modifiers for the three lubricating regimes [13].

A very popular and widely used solid lubricant that has been used in many different forms including as a dry lubricant applied directly to surfaces, dispersed in oils or greases and even used in self-lubricating composite components is the inorganic compound molybdenum disulphide (MoS_2) [6, 7, 17, 19, 20, 21]. For many years MoS_2 has been used and is still a popular choice in numerous applications such as metalworking, nuclear power plants, aerospace components, and automotive lubrication [16, 20]. MoS_2 is well known for its lubricating properties in applications involving heavy loads [17, 22]. MoS_2 is one of the softest materials with a value of 1.0 - 1.5 on Mohr's scale [5]. The lubrication quality of MoS_2 (as with graphite)

is widely attributed to the fact that it is a layered structure [17, 22, 23, 24]. However, having a layered structure does not necessarily imply a material will have a low coefficient of friction or good lubrication properties. For example, compounds such as CdI_2 and $Ca(OH)_2$ also have layered structures but are poor lubricants [17, 23].

The molybdenum atoms have a polarization effect on the sulfur atoms. This leads to strong covalent bonding within a S-Mo-S layer and relatively weak attractive forces between the S-Mo-S layers. This is also the reason for the arrangement of the MoS_2 crystal structure and therefore the anisotropic cleavage and weak shear forces required to remove an S-Mo-S layer [17, 23, 24]. More details on MoS_2 are provided in Section 1.2. In comparison, the CdI_2 and $Ca(OH)_2$ compounds have covalent and ionic bonds and no polarization effects within the crystal, which does not provide for the easy shearing of layers [23].

The importance of MoS_2 as a lubricant has lead to significant fundamental and applied research [24], in particular, the study of the effects of operating and environmental conditions on the frictional properties of MoS_2. A brief review of this work is provided below. The tribological properties of MoS_2 can be affected by many factors such as purity, particle size, humidity and temperature [20, 24]. A more detailed review of MoS_2 as a lubricant and its behavior under certain environmental conditions such as water vapor, temperature, vacuum, radiations, chemical effects, varying loads, etc. can be found in [17, 23, 24]. Papers that discuss the frictional modification properties of MoS_2 when added as a friction modifier to various lubricants can be found in [3, 18, 19, 20, 21, 22, 25].

In 2008, Verma *et al.* [26] investigated the tribological behavior of MoS_2 nanoparticles, synthesized in different conditions, as an additive to paraffin oil. These nanoparticles were designed to be intercalated with organic molecules, specifically canola oil, and lecithin as a

phosphorous source. These nanoparticles were developed specifically to be nano-sized and intercalated with canola oil and lecithin so that the particles would be able to traverse the nano- to micro- sized surface asperities to deliver lubricating films to the area where micro-sized additives were insufficient during surface sliding in extreme temperatures and pressures [26]. The specific reason for including lecithin is that it includes phosphorous. Phosphate molecules are exceptional anti-wear agents and were included in the MoS_2 additive mixture so that they may be selectively applied to rubbing surfaces when the nanoparticles are sheared and removed during high-pressure use [26]. When these molecules are deposited at high pressures, the surfaces are still protected therefore reducing friction and preventing wear and seizure [26]. A schematic of a MoS_2 nanoparticle with the intercalated fatty acids can be seen in Figure 1.4.
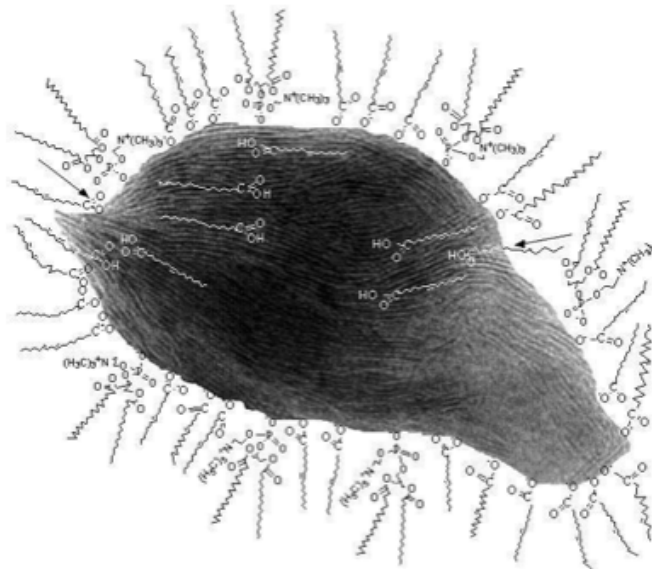
Figure 1.4: A schematic of a MoS_2 nanoparticle intercalated with fatty acids [5].

In the study by Verma *et al.* [26] two types of lubricants were tested. One lubricant was pure paraffin while the other lubricant had MoS_2 nanoparticles dispersed in the paraffin oil. The lubricant with MoS_2 as an additive was broken into three samples. The first sample was prepared

with commercially available MoS$_2$ particles (c-MoS$_2$). The second was prepared with dry (in air) ball milled MoS$_2$ (d-MoS$_2$) particles dispersed in the paraffin oil. The third sample was prepared with MoS$_2$ particles (h-MoS$_2$) that were first dry ball milled in air and then ball milled in canola oil. In all three samples, MoS$_2$ was present at 1.0% concentration by weight in the paraffin oil. These four lubricants were tested with a four-ball tribometer to test their effectiveness in (i) reducing the wear scar diameter created during loading, (ii) reducing the coefficient of friction, and (iii) their performance at extreme pressures. Figure 1.5 shows a graph of wear scar diameters (WSD) created for each of the tested lubricants. The graph shows that the lubricants containing c-MoS$_2$ and d-MoS$_2$ additives had a minor effect on the wear scar diameter created.
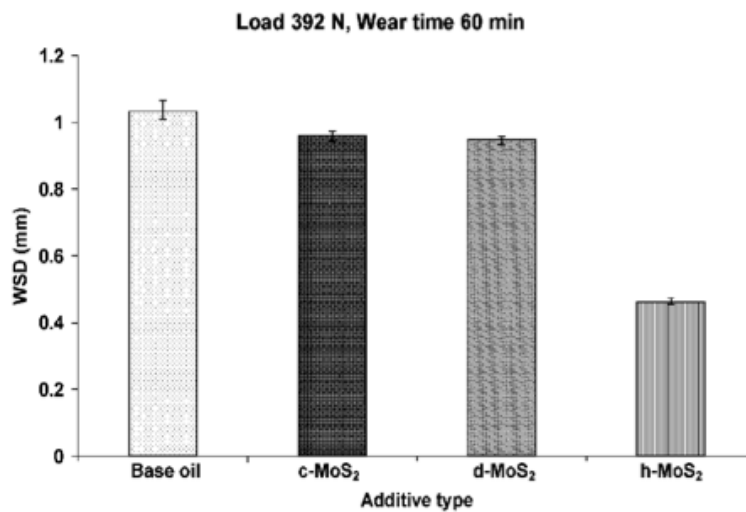
Figure 1.5: Reduction in WSD for MoS$_2$ additives [26].

The wear scar diameter decreased from 1.03 mm in the pure paraffin oil case to 0.96 mm (c-MoS$_2$) and 0.95 mm (d-MoS$_2$). Also seen in the graph is the significant reduction in the WSD for the lubricant with the hybrid milled MoS$_2$ additive (h-MoS$_2$). With h-MoS$_2$, the WSD decreased to 0.46 mm (more than a 50% decrease). As shown in Figure 1.5, and as was expected,

the pure paraffin oil produced the highest coefficient of friction. The lubricants with MoS_2 additives clearly produced a reduction in the COF while the h-MoS_2 lubricant produced the lowest COF at 0.069. A summary of the wear scar diameters and coefficients of friction for their study can be found in Table 1.

Solid Lubricant × % dispersions	Particle/cluster size	Four Ball Tests at 392N Load (ASTM D-4172)*	
		WSD (mm)	COF
Base oil	N/A	1.033	0.155
c-MoS_2 (1.0 %)	3-5 μm/25 μm	0.960	0.114
d-MoS_2 (1.0 %)	<100nm/1 μm	0.948	0.091
h-MoS_2 (1.0 %)	<100nm	0.461	0.069

Table 1.1: Summary of WSD and COF reduction with MoS_2 additives [26].

In studying the effects of extreme pressure on these lubricants, Verma *et al.* [26] also created lubricants with different amounts of added MoS_2; MoS_2 was added at 0.5%, 1.0% and 1.5% concentration by weight to the paraffin oil for each of the three types of MoS_2 particles. Verma *et al.* [26] reported that the c-MoS_2 and d-MoS_2 lubricants had no effect on the COF during the tests. This was attributed to the nanoparticles not being ideally suspended in the oil and becoming clumped together in sizes of ~10 microns. These micron-sized particles were not able to easily travel around the surface asperities during rubbing to deposit a protective lubricating film. However, the h-Mos_2 lubricant had a significant impact as seen in the graph. In this case, the lubricant was able to support a higher load before seizure. This was because the nanoparticles were well suspended in the oil without any clumping occurring [26].

Studies of the tribological performance of MoS_2 and MoS_2 as an additive can be found in the following references [3, 6, 16, 18, 19, 20, 21, 22, 25, 27]. The incorporation of MoS_2 as an

additive in lubricants plays a role in increasing the tribological properties of the lubricant, facilitating the development of a durable lubricant in the boundary lubrication regime. This allows for a reduction in friction, a reduction of component wear during use, and therefore will lead to an increase in energy efficiency. However, further research on the fundamental aspects of the physical and chemical behavior of MoS_2 needs to be done. Some aspects that need to be investigated with regards to MoS_2 and intercalated MoS_2 particles are: (i) the chemistry dependent properties of the MoS_2 nanoparticles when they are intercalated with organic fatty acid chains; (ii) the friction and wear experiments to investigate the behavior of the additives suspended in oils at the surface under high pressure conditions; and (iii) to study the defect based mechanisms associated with mechanical deformation encountered in boundary lubrication to explore the size and strain affects of these defects on the frictional characteristics of MoS_2.

1.2   Molybdenum Disulphide

The impressive tribological properties of molybdenum disulphide (MoS_2) are attributed to its lamellar and hexagonal crystal structure (more rarely in a rhombohedral crystal structure) created from the polarization and covalent bonding effects described in Section 1.1. A schematic and TEM image of the layered MoS_2 crystal structure is shown in Figure 1.7. The layered structure of MoS_2 can clearly be seen in Figure 1.7b.

Each molybdenum (Mo) atom is surrounded by six sulfur (S) atoms that create a trigonal prism [17, 28]. Since Mo atoms have a strong polarization effect on the S atoms, covalent bonds are created between the Mo and S atoms within a S-Mo-S tri-layer. Since the S atoms are polarized, the surface of the sulfur layer has a distribution of weak dipoles. This distribution leads to the stacking of the S-Mo-S structures and a weak van der Waals attractive force between

the S-Mo-S tri-layers. This van der Waals attraction between the S-Mo-S layers leads to the easy cleavage of MoS_2 and therefore good frictional characteristics [17, 23, 24]. The experimentally determined lattice constants of MoS_2 are a = 3.16 Å and c = 12.29 Å with a bond length for Mo-S is 2.42 Å [28]. The in-plane S-S and Mo-Mo distance in a layer is 3.16 Å. The S-S distance between tri-layers is 3.49 Å. The distance between interlayer S-S planes is 2.92 Å.
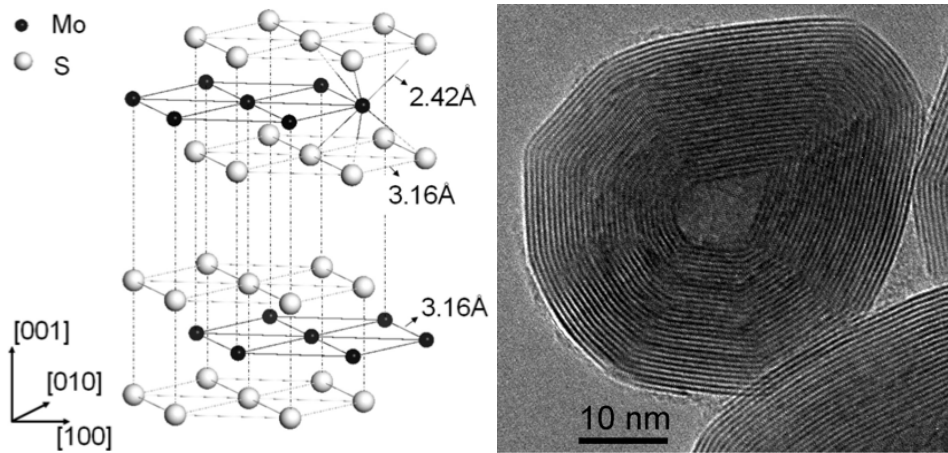
Figure 1.6: (a) Schematic of MoS_2 crystal structure [28]
(b) TEM Image of MoS_2 nanostructure [29].

MoS_2 has a very low coefficient of friction between 0.01 and 0.08 depending on load and the environment. In vacuum, the coefficient of friction is reduced to 0.002 [21, 25]. Again, this low friction property is due to the layered structure and atomic bonding of MoS_2. MoS_2 is considered an "extreme pressure" lubricant and is therefore used in conditions where severe operating conditions and extreme pressures occur [17]. Between 0°C and 100°C, at constant load, the coefficient of friction decreases with increasing temperature. At temperatures above 700°C, MoS_2 will react with steel surfaces, which creates another layer of protecting and lubricating film [17]. The melting temperature of MoS_2 is very high at 1185°C [30], which makes it an appropriate choice for extreme temperature applications. In general, MoS_2 does not react unless

it is physically or mechanically forced to react (i.e., "activated") at high temperatures or pressures.

With MoS_2, it is essential to understand, at the atomic level, the formation, propagation, and interaction mechanisms of defects and how these defects may alter the tribological performance of MoS_2. During synthesis or application of the nanoparticles deformation will occur, necessitating defects and dislocation nucleation [14]. As such, this work focused specifically on modeling the mechanisms associated with defect nucleation and intralayer fracture in crystalline MoS_2 nanoparticles at the atomic level via mechanical deformation. Modeling this process at the atomic level provided insight into the structure-property relationship of defects and the tribological performance of MoS_2.

While a tremendous amount of experimental work has been done to investigate the frictional characteristics of MoS_2 as a stand-alone lubricant and as an additive, there have also been computational studies focused on MoS_2. With increasing computational power and capabilities being developed, computational materials modeling is becoming more popular and widespread as a predictive tool [31]. These computational studies have included atomistic simulations and quantum mechanical calculations to study the structural, mechanical, electronic, and frictional properties of crystalline MoS_2.

Wei *et al.* [32] used density functional calculations to calculate the band gap energy, density of states, lattice and elastic constants at pressures from 0 - 40 GPa. Wei *et al.* [32] reported a band gap energy of 0.79 eV, which they report is smaller than previous values in the literature of 1.2 - 1.29 eV. This underestimation is a known drawback of the method employed in their work. At 0 GPa, Wei *et al.* [32] calculated MoS_2 lattice parameters of a = 3.199 Å, c = 12.493 Å, a Mo-S bond length of 2.41 Å and elastic constants of C_{11} = 211.2 GPa and C_{33} = 36.7

GPa. They also determined that as the pressure was increased from 0 GPa to 40 GPa the band gap and lattice constants decreased to 0.4 eV, a = 2.955 Å and c = 10.71 Å while the elastic constants increased to C_{11} = 418.326 GPa and C_{33} = 382.437 GPa. Chermette *et al.* [33] also carried out density functional calculations to study the changes in the electronic structure and the frictional properties of MoS_2 due to the oxidation of MoS_2 and the substitution of sulfur by oxygen.

Weber *et al.* [34, 35] implemented density functional calculations to study the structural and elastic properties of MoS_2 and the adsorption of lithium ions on the $(10\bar{1}0)$ face of a MoS_2 crystal. The adsorption study was done to address the catalytic properties of MoS_2 since MoS_2 is commonly used as a catalyst in hydrodesulphurization of oil. They compared the results of various density functional methods to find the best description of MoS_2. Weber *et al.* [34] reported that the use of Hartree-Fock with the Perdew-Wang Generalized Gradient Approximation (HF + DW-GGA) provided the best results for reproducing lattice and elastic constants. Using this HF + DW-GGA method, they report lattice constants of a = 3.1 Å, c = 12.4 Å and elastic constants of C_{11} = 255.05 GPa and C_{33} = 35.37 GPa (experimental values of C_{11} = 238 GPa and C_{33} = 52 GPa).

Stefanov *et al.* [36] used density functional calculations to study the effects of high compressive loads on the frictional properties of multi-walled MoS_2 nanotubes. They found, in all of the nanotube cases, that as the applied load from a rigid substrate increased, the MoS_2 nanotubes would irreversibly deform and fracture. Once the nanotubes fractured, they began to organize themselves into layered structures onto the surfaces of the substrate. The organization of MoS_2 onto the substrate in a layered form was indicative that MoS_2 may provide a lubricating film during high loads and the mating surfaces will never come into contact. The authors also

14

stated that their findings showed it might be possible to "tune" the mechanical properties of MoS$_2$ nanostructures to create nano-coatings during the use of MoS$_2$ as a lubricant.

Varshney *et al.* [37] used molecular dynamics simulations to model the thermal transport behavior of MoS$_2$ in directions parallel and perpendicular to the basal plane. The interatomic potential used by Varshney *et al.* [37] included bonded, angle, and non-bonded interactions for the MoS$_2$ crystal. In each simulation, the "hot" end of the crystal was held at 350 K while the "cold" end was held at 250 K. In each simulation direction, Varshney *et al.* [37] found the temperature profile of the MoS$_2$ lattice to be linear (the temperature linearly decreased from hot to cold across the simulation cell). The thermal conductivity was also calculated for these to direction. The thermal conductivity for the parallel direction was calculated to be 18.06 ± 1.42 W/m-K (experimental values of 1.2 - 1.5 W/m-K) while the perpendicular direction was calculated to be 4.17 ± 0.36 W/m-K (experimental values of $0.2 - 0.5$ W/m-K). Varshney *et al.* [37] stated that the reason the computational results were higher than experimental values was because of their use of small (7,680 - 9,216 atoms) and ideal model MoS$_2$ crystals. The anisotropy in the thermal conductivity is a result of the multi-layered structure of MoS$_2$.

Morita *et al.* [38] developed a molecular dynamics program to study the formation of MoS$_2$ structures on iron surfaces (compressed and sliding) from initially amorphous MoS$_2$ and their frictional properties. To model interatomic interactions, an interatomic potential was used that included bonded, angle, Coulomb, and van der Waals interactions. A simulation cell of size 27.5 Å x 27.5 Å x 100 Å was used where the iron substrate applied a compressive load of 0.5 GPa. During the simulation, Morita *et al.* [38] found that the amorphous MoS$_2$ would self-organize into layered structures in the iron surface. They also found that the COF significantly decreased from ~ 0.3 near the beginning of the simulation to 0.006 at the end of the simulation.

Brunier *et al.* [39, 40] developed an interatomic potential for the MoS₂ structure that included bonded, non-bonded, angle and torsional interactions and was fit to experimentally determined lattice constants. Molecular mechanics (statics) calculations were then used to study the structure of crystalline MoS₂, specifically the Mo-S bond lengths on a system of 181 atoms. They were able to accurately reproduce the hexagonal MoS₂ structure with a Mo-S bond length of 2.419 Å. They then used this same interatomic potential and molecular mechanics approach to study the catalyst effects of MoS₂ with the binding of thiophene to open (or "active") sites on ($\bar{1}$010) and (10$\bar{1}$0) surfaces.

Liang *et al.* [28] parameterized a reactive bond order potential specifically for Mo-S systems to study the frictional property of a MoS₂ structure sliding on a MoS₂ substrate. They studied a small (551 atoms) MoS₂ layer sliding on top of a larger (11,520 atoms) MoS₂ substrate with a simulated compressive load of 2 GPa. As the smaller structure slid across the substrate, the displacement of the layer and changes in the perpendicular and parallel forces were determined. Knowing the perpendicular ($F_\perp$) and parallel ($F_\parallel$) forces allowed determination of the average COF [27, 28] i.e.,

$$\mu = \frac{F_\parallel}{F_\perp}$$

Equation 1.1

In the study by Liang *et al.* [28], an average COF was calculated to be 0.17, which agreed very well with experimental data. This potential was developed specifically to study the tribological performance of MoS₂ and was proposed to use this potential to gain insight into the structural and frictional characteristics of MoS₂.

While these previous computational studies provide useful information about the properties of MoS₂, they do have their limitations, especially in being able to study mechanical

deformation and defect formation in MoS_2. The number of atoms that can be modeled limits quantum mechanical calculations. While this limitation is fine for calculating electronic structures it is not very useful in modeling and predicting bulk material behavior. The molecular dynamics or molecular mechanics simulations remove this limitation by being able to model up to billions of atoms [41]. The limitation here comes from the interatomic potentials that are used in the simulation. The potential of Brunier *et al.* [39] is limited in the fact that bond and angles have to be defined prior to the simulation. This means that there is no reactive component to the potential since the atoms stay bonded to their initial neighbors during the whole simulation, which provides unrealistic energies and forces. Therefore, with these types of potentials, it is not feasible to model bond breaking, bond formation and intralayer fracture. The ability to allow for bond breaking is essential for studying defect nucleation and motion.

As such, this work focused on using the parameterized potential of Liang *et al.* [28] that provides a reactive component to the simulation. This work provides an advancement to previous work since the reactive ability of this potential allowed the simulation to accurately capture bond breaking and formation as well as defect movement during deformation of the MoS_2 crystal. To this date, there have been no efforts reported in the literature to study the fundamental mechanisms of defect nucleation and interaction as well as intralayer fracture in crystalline MoS_2. Understanding the impact of defects and intralayer fracture on the frictional properties of MoS_2 is crucial to allow the design and synthesis of durable, reliable, and predictable nanoparticle MoS_2 additives for lubricants.

1.3   Thesis Objectives

There were two main objectives to this thesis: (i) to implement a modified bond order interatomic potential for Mo-S systems into an atomistic simulation package and (ii) to use this potential and molecular statics calculations to investigate defect nucleation and intralayer fracture by nanoindentation on the basal plane of crystalline MoS_2 which together they provided insight into the formation of defects during nanoparticle synthesis or application of the nanoparticles in lubricating conditions.

First, a reactive empirical bond order (REBO) interatomic potential that has been modified and parameterized for Mo, S and Mo-S (specifically MoS_2) systems was incorporated into LAMMPS (Large-scale Atomic Molecular Massively Parallel Simulator), a classical molecular simulation package. It was important that the implemented interatomic potential calculate atomic energies and forces that were consistent with the derived energy and force equations (discussed in Chapter 3) as well as calculating the exact energy and force quantities that the Liang *et al.* [28] atomistic code calculates. Liang *et al.* [28] graciously provided their atomistic code for direct comparison with the LAMMPS implementation. In order to assure that the Mo-S potential was properly implemented into LAMMPS, atomic energies and forces as well as structural information including lattice and elastic constants were directly compared from the original Liang *et al*. [28] atomistic code and the LAMMPS code for small test structures. It was crucial to verify that LAMMPS properly reproduced information about the MoS_2 structure so that atomic processes could be accurately captured. Accurately capturing these processes allowed precise predictions and conclusions to be drawn during mechanical deformation processes.

Second, atomistic simulations of nanoindentation on the basal plane of crystalline MoS_2 were done to study defect formation mechanisms and intralayer fracture in this material under

mechanical deformation. This simulation was done using molecular statics (at zero temperature and therefore no kinetic energy) to keep the system in its minimum energy state (i.e., the relaxed crystal structure). A frictionless indenter was used to simulate the nanoindentation process. Molecular statics and a frictionless indenter were used in the simulations so that definitive conclusions could be made about the defect nucleation process of crystalline MoS_2 without the influences of temperature and interactions with the indenter tip. These simulations were done with varying sizes of the indenter diameter. Figure 1.7 shows a schematic of the atomistic simulation geometry that was used for the nanoindentation process.
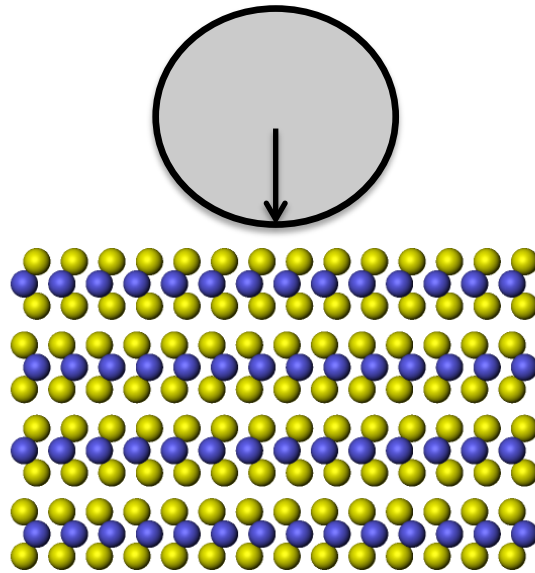
Figure 1.7: Schematic of the atomistic simulation geometry used to study defect nucleation during nanoindentation of MoS_2 (Mo = Blue, S = Yellow).

These calculations provided an understanding of: (i) the forces required to break bonds and (ii) the mechanism by which defects formed and propagated within the lattice; specifically, if the mechanism associated with defect formation and deformation during mechanical contact was the occurrence of broken bonds, which is the hypothesized failure mechanism.

CHAPTER 2:   THEORY OF ATOMISTIC SIMULATION

2.1   Introduction

Atomistic simulation is a method of modeling materials or a configuration of atoms and their properties at the atomic level. Atomistic simulations generally fall into three categories: Monte Carlo, molecular dynamics simulations and molecular mechanics (statics). These techniques make it possible to study physical configurations and assist in the development of experiments and theories. Atomistic simulations can [42 - 48]:

(i)   provide insight into the behavior of physical systems where theoretical approximations are untested as well as testing the validity of approximations against known model systems

(ii)   simulate conditions that may not be experimentally available or systems that are not seen in nature

(iii)   provide visualization of specific processes to study complex phenomena

(iv)   provide assistance in understanding existing materials and designing new materials

In this work, the term atomistic simulation will specifically refer to the molecular mechanics (statics) technique. Section 2.2 will provide a brief discussion of the molecular statics technique used in this work. Detailed descriptions of Monte Carlo methods, molecular dynamics, and other techniques used within these simulation methods can be found in textbooks by Allen and Tildesley [43] and Frenkel and Schmidt [45] and in references [42, 44, 46, 47, 48].

In an atomistic simulation, the atoms are represented as point particles in a configuration space with mass, m. An interatomic potential function, U, provides an approximate model of the

interaction energy of the system of atoms. A common aspect of interatomic potentials is that they do not explicitly include the interactions associated with individual electrons. Instead, the potential energy of the system is generally determined exclusively as a function of the atomic positions. These simplifications make it computationally feasible to model large systems of atoms. Using the interatomic potential function, U, it is possible to calculate the force on any given atom. The force, $\mathbf{F}_i$, on the ith atom due to its neighbors is determined by the negative gradient of the potential function i.e.,

$$\mathbf{F}_i = -\frac{\partial U}{\partial \mathbf{r}_i}$$

Equation 2.1

In Equation 2.1, $\mathbf{r}_i$ is the atomic position vector for the ith atom. A detailed discussion of the interatomic potentials used in this work will be presented in an overview in Section 2.3 and specifically for MoS_2 in Section 3.2.

One of the limitations of atomistic simulations is that models are limited to relatively small systems of atoms because of computational resources [43, 44, 46]. This implies that one cannot model realistic macroscale system with a large number of atoms (on the order of Avogadro's number of atoms). To alleviate this problem, periodic boundary conditions are used. Figure 2.1 shows a two dimensional illustration of periodic boundary conditions used in atomistic simulations.

The primary cell is located in the center of Figure 2.1 and contains atoms within it that represent a small portion of a material. The atoms located in this primary cell are modeled using atomistic methods. The bordering cells contain replica images of the primary cell and atoms being studied. These image cells are periodically repeated to simulate an infinite crystal lattice.

21
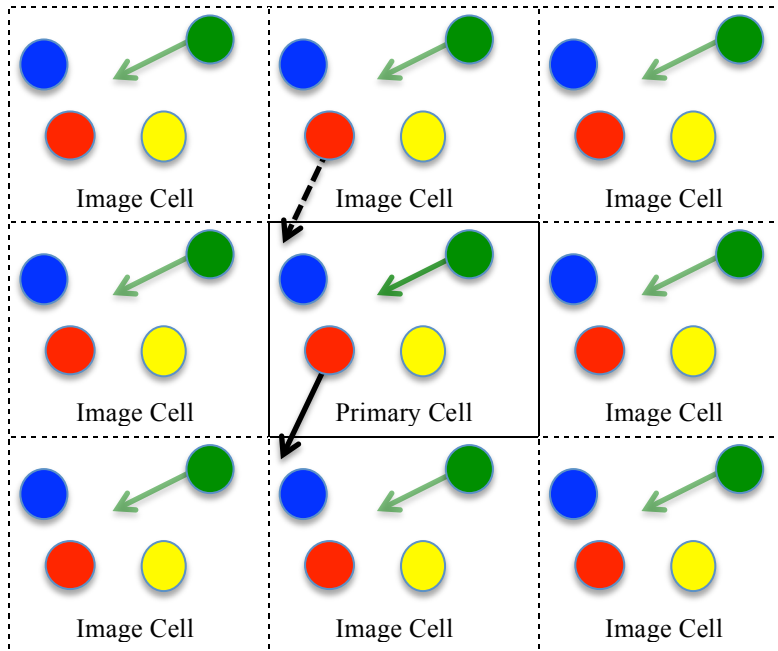
Figure 2.1: Illustration of Two-Dimensional Periodic Boundary Conditions.

As a particle within the primary cell moves during the simulation as described by the interatomic potential or by an external force, its corresponding image atom in all image cells will move in exactly the same way; as shown by the green atoms in Figure 2.1. If a particle were to leave the primary simulation cell, its image would enter the primary simulation cell through the opposite cell face with the same properties as the original primary atom. For example, suppose the red atom located in the primary cell moves outside of the primary cell, as illustrated in Figure 2.1 with a solid arrow. The image of this atom will move into the primary cell through the opposite side of the cell, as shown with a dotted arrow in Figure 2.1. Atoms that are located near the boundary of the primary cell will interact with atoms across this boundary. As a result, there are effectively no walls constraining the primary cell, which gives the effect of an infinite lattice with the constraint that the number of atoms, N, must be conserved. These periodic boundary conditions can also be problematic in the case of long-range interactions where an atom could interact with its own image through the boundary [43]. This constraint needs to be taken into

consideration when simulating defect behavior. If periodic boundary conditions are used in three dimensions, then it is possible to remove any surface effects.

The atomistic simulation code used in this work (LAMMPS) [49] was written by Steve Plimpton, Aidan Thompson and Paul Crozier at Sandia National Laboratories / Albuquerque, NM. The current version of the code is written in C++ and can be used on a single processor or on multiple processors by the use of message passing techniques and a spatial decomposition of the simulation cell. LAMMPS has a library of implemented interatomic potentials that allows the modeling of biomolecules, polymers, metals and semiconductors and the capability to simulate frictionless spherical indentation. In order to accurately model crystalline MoS_2 and the nanoindentation of MoS_2, it was necessary to modify specific subroutines in the LAMMPS code. The changes implemented into LAMMPS are: (i) the angular and coordination spline functions from the original REBO potential were replaced with polynomials, (ii) the coordination function was changed to allow for a pair of atoms (the ith and j^{th} atoms) to have a force interaction within the bond-order function and (iii) to modify the Lennard-Jones interaction at small interatomic distances with an implemented spline function to terminate the Lennard-Jones interactions below a minimum cutoff distance. A more detailed discussion of these changes is given in Chapter 3.

2.2   Molecular Statics

One of the most common tasks in atomistic simulations is to find the stable equilibrium configuration of a given system of atoms or crystal structure. This corresponds to finding an atomic structure (close to the desired crystal structure) with a minimum potential energy [50]. In this work, molecular statics (MS) calculations were used to compute the minimum energy structure (the relaxed state) of the MoS_2 crystal, within a given tolerance. The conjugant gradient

(CG) method was used to determine the minimum potential energy structure of MoS_2. A brief overview of the conjugant gradient method is provided in the following discussion. A more detailed review of the conjugant gradient method that follows can be found in Shewchuk [51].

The most prominent method for solving sparse systems of linear equation is the method of conjugant gradients [51]. Given a function $f(x)$, if $f(x)$ is continuous, has a minimum and its derivative exists (i.e., it can be calculated) then the method of conjugant gradients can be used to find the minimum of $f(x)$. The general concept of the conjugant gradient method is to start at an initial location on the surface of a function $f(x)$ and repeatedly move in conjugant directions until the minimum of $f(x)$ is determined. In atomistic simulations, this corresponds to moving atomic positions over the potential energy surface (the interatomic potential function $U(\mathbf{r})$) until they reach a minimum potential energy configuration. From Equation 2.1, we know that the force vector is determined by the negative gradient of the potential energy function, $U(\mathbf{r})$. From calculus, the gradient of a function points in the direction of steepest increase of a function. Since the force vector is the negative of the gradient, the force vector points in the direction of steepest decrease of a function. In the conjugant gradient method, a quantity called the residual is defined. The residual determines how far the current approximate solution to the minimum is to the correct solution for the minimum, similar to the error. Therefore, in atomistic simulations, the residual is defined to be:

$$\mathbf{g}_m = -\frac{\partial U(\mathbf{r})}{\partial \mathbf{r}_m} \qquad \text{Equation 2.2}$$

In Equation 2.2, m denotes the mth iteration in the conjugant gradient method. By comparing Equations 2.1 and 2.2, it is clear that the residual is equivalent to the force vector. Therefore, the

force vector is the residual associated with the potential energy function. With the residual defined, the atomic positions can be updated or moved to the potential energy minimum by an iterative process given by:

$$\mathbf{r}_{m+1} = \mathbf{r}_m + \alpha_m \mathbf{d}_m$$

<div align="right">Equation 2.3</div>

In Equation 2.3, α is a scalar that minimizes the potential energy along the current (m[th]) search direction and $\mathbf{d}$ is the current (m[th]) search direction that α is chosen to minimize along. In the conjugant gradient method, the first search direction is taken to be the residual itself i.e.,

$$\mathbf{d}_0 = \mathbf{g}_0 = -\frac{\partial U(\mathbf{r})}{\partial \mathbf{r}_0}$$

<div align="right">Equation 2.4</div>

To determine the alpha that minimizes the potential function, the derivative of the potential function, U, at the point $\mathbf{r}_{m+1}$ (Equation 2.4) is set to zero. Doing this requires the residual at $\mathbf{r}_{m+1}$ and the search direction $\mathbf{d}_m$ to be orthogonal i.e.,

$$(\mathbf{g}_{m+1})^T \mathbf{d}_m = 0$$

<div align="right">Equation 2.5</div>

In the conjugant gradient method, to calculate the value of α that minimizes the potential function in the search direction, $\mathbf{d}_m$, and satisfies Equation 2.5, a line search procedure is commonly used. Common line search techniques are Newton-Raphson, Secant and backtracking methods. The backtracking line search algorithm is the method incorporated in LAMMPS, which

is computationally efficient since the gradient of the potential function does not need to be calculated.

As stated above, the first search direction in the conjugant gradient method is taken to be just the residual of the potential energy function, Equation 2.4. With this initial search direction and α, the atomic positions are updated from their initial positions, $\mathbf{r}_0$, to new positions, $\mathbf{r}_1$. With the new positions determined and using Equation 2.2, a new residual can be calculated. To iterate this process, each following search direction is constructed from the new residual and the previous search direction (the search directions are constructed by conjugation of the residuals [51]) and is given by:

$$\mathbf{d}_{m+1} = \mathbf{g}_{m+1} + \beta_{m+1}\mathbf{d}_m \qquad \text{Equation 2.6}$$

These new search directions are determined from the previous search direction by use of the parameter β. The values of β are chosen so that each successive search direction is conjugate to the previous search direction with respect to U (or U-orthogonal) [51] i.e.,

$$(\mathbf{d}_{m+1})^T U \mathbf{d}_m = 0 \qquad \text{Equation 2.7}$$

There are two methods to estimate the value of β: the Fletcher-Reeves and Polak-Ribiere formulas. The Polak-Ribiere formula has better convergence properties over the Fletcher-Reeves formula and is the method used in the LAMMPS code. It is given by:

$$\beta_{m+1}^{PR} = max \left\{ \frac{\mathbf{g}_{m+1}^{T}(\mathbf{g}_{m+1} - \mathbf{g}_m)}{\mathbf{g}_m^{T}\mathbf{g}_m}, 0 \right\}$$

<div align="right">Equation 2.8</div>

Convergence of the Polak-Ribiere method is guaranteed by choosing β^{PR} with Equation 2.8 [51]. Note that if $\beta = 0$, the method of steepest decent is recovered (and the search directions become just the residual of the potential energy function). The method of conjugant gradients is an advancement upon the steepest decent method because in steepest decent numerous steps can be taken in the same search direction whereas conjugant gradients limits one step in each conjugant search direction.

2.3   Interatomic Potentials

In atomistic simulations, it is necessary to calculate the forces acting on each atom to predict the evolution of the configuration. The atomic energies and forces are calculated with the use of an interatomic potential. As such, the success of an atomistic simulation is determined by the accuracy of the interatomic potential used. Although there is a trend to use accurate quantum mechanical methods for interatomic interactions, this method is restricted by computational resources to small systems and large computing times. Examples of material properties that are too complex to use quantum mechanical method are: surface phase transitions, grain boundary structure and dislocation motion [44]. Therefore, an interatomic potential that is fit to material properties that capture the underlying atomic processes is used. These empirical interatomic potentials are designed to allow easy and rapid calculation of interatomic forces to model large systems of atoms and the above problems become easy to study [44, 52].

Generally, interatomic potentials can be categorized into four different classes: (i) pair potentials, (ii) cluster potentials, (iii) pair functionals and (IV) cluster functionals [53]. These

classes of interatomic potentials have an increasing level of complexity. The increasing level of complexity in these potentials allows for a more accurate description of the interatomic interactions and therefore a better model of material properties. In the simplest class, the pair potentials, the force between a given pair of atoms is only a function of the separation distance of these two atoms. These simple pair potentials do not incorporate the environment (location and number of neighbors) of an atom to alter the interaction of a pair of atoms. In the most complex potential class, the cluster functionals incorporate sophisticated descriptions of the local environment of an atom in determining the interatomic interactions [53]. A more detailed review of interatomic potentials can be found in Carlsson [53] and Finnis [54]. Sections 2.3.1 and 2.3.2 will provide a brief discussion of the reactive empirical bond order (REBO) and Lennard-Jones interatomic potentials, as they are critical to this research.

2.3.1   The Reactive Empirical Bond-Order (REBO) Interatomic Potential

Abell first developed an analytic form for the reactive bond-order potential in 1985 to describe metallic and covalent bonding [55]. This bond-order potential models the attractive contributions to the potential energy through the use of a many-bodied bond-order function. This bond-order function controls the strength of the pairwise interactions by being a function of the local environment of a given atom. According to Abell, the coordination of an atom is the major component in determining the bond-order function [52, 55]; for example, an atom with many neighbors forms weaker bonds than an atom with few neighbors. With the bond-order potential in place, Tersoff [56, 57, 58] advanced Abells bond-order formalism to provide a better model of atomic environments and therefore a better description of bonding energies for realistic covalent systems of different bonding geometries. Brenner *et al.* [52, 59] developed a second-generation

reactive bond-order potential, which gave a better description of bond energies, bond lengths, elastic properties, defect and surface energies for hydrocarbons and diamond. Stuart *et al.* [60] extended this reactive bond-order potential of Brenner even further to include non-bonded and torsional interactions. This potential is empirical in that it is fitted to data from experiments or quantum mechanical calculations. This potential has been parameterized (fitted) to study silicon, carbon, germanium, hydrocarbons and fluorocarbons [57, 58, 59, 61, 62]. The REBO potential has been used to study many problems such as growth of hydrocarbon thin films [63], tribological properties, fracture and nano-indentation carbon of nanotubes [64, 65]. The REBO potential has been shown to always be qualitatively accurate when compared to quantum mechanical methods an often quantitatively accurate [66]. The following will provide a brief overview of the second-generation reactive bond-order potential of Brenner *et al.* [52, 59], which was the basis of the parameterized Mo-S REBO potential discussed in Section 3.2.

Brenner *et al.* [52, 59] developed the REBO potential to (i) be computationally efficient, (ii) provide better descriptions of bonding energies, force constants and bond lengths for carbon and hydrocarbon systems as well as being transferable to other systems and (iii) allow for bond breaking and formation of covalent bonds. In the REBO potential, the potential energy is written as the sum over the nearest neighbors of an atom i.e.,

$$U = \sum_{i<j} f^c(r_{ij})\big[V^R(r_{ij}) - b_{ij}V^A(r_{ij})\big]$$

$$= \sum_{i<j} f^c(r_{ij})\left[\left(1 + \frac{Q_{ij}}{r_{ij}}\right)A_{ij}e^{-\alpha_{ij}r_{ij}} - b_{ij}\sum_{n=1,3} B_{ij}^n e^{-\beta_{ij}^n r_{ij}}\right] \qquad \text{Equation 2.9}$$

In Equation 2.9, r_{ij} is the interatomic separation distance between atoms i and j; f^c is a cutoff function that limits the atomic interactions to first and possibly second nearest neighbors; V^R and V^A are pairwise functions that model the repulsive and attractive atomic interactions, respectively; and b_{ij} is the many-body bond-order term that is a function of the local environment (coordination and angular interactions) of an atom and modifies the pairwise interactions accordingly. The parameters α_{ij}, β_{ij}, A_{ij}, and Q_{ij} are pairwise parameters that depend on the atom types of atom i and atom j and are fit to reproduce specific material properties. The parameter Q_{ij} can be regarded as the screened Coulomb interaction [52]. The bond-order term is given by:

$$b_{ij} = \frac{1}{2}\left[b_{ij}^{\sigma-\pi} + b_{ji}^{\sigma-\pi}\right] + b_{ij}^{\pi} \qquad \text{Equation 2.10}$$

The $b_{ij}^{\sigma-\pi}$ and $b_{ji}^{\sigma-\pi}$ terms are functions of the local environment of an atom, the angular interactions and the local coordination of an atom. The $b_{ij}^{\sigma-\pi}$ term (similarly for $b_{ji}^{\sigma-\pi}$) has the expression:

$$b_{ij}^{\sigma-\pi} = \left[1 + \sum_{k\neq i,j} f_{ik}^c(r_{ij})\text{G}(\cos(\theta_{ijk}))\,e^{\lambda_{ijk}} + P_{ij}(N_i^C,N_i^H)\right]^{-1/2} \qquad \text{Equation 2.11}$$

In Equation 2.11, f_{ik}^c is a cutoff function that limits the angular interactions to first and possibly second neighbors with the summation excluding the i-j angular interaction. The function $\text{G}(\cos(\theta_{ijk}))$ accounts for the angular interactions of a set of atoms i, j and k. The parameter

30

λ_{ijk} is used to provide a smooth potential energy surface by removing false energy wells that would cause unrealistic attractions to occur in certain geometries. The function, P_{ij}, depends on the coordination number of an atom where N_i is the number of neighbors of atom i. The function b_{ij}^{π} is written as:

$$b_{ij}^{\pi} = \Pi_{ij}^{RC} + b_{ij}^{DH} \qquad \text{Equation 2.12}$$

In Equation 2.12, the b_{ij}^{DH} term is a function that describes rotational forces associated with dihedral angles while the Π_{ij}^{RC} term accounts for energy influences from atoms that have open electron shells (radical energies) and systems where a p-orbital overlaps a σ-bond or double bonded states (π-bond conjugated systems) [52, 59].

In the REBO potential, the local environment of an atom determines the interatomic interactions. As such, atomic bonding in this potential is described by the local bonding of nearest neighbors and non-local double bonding effects [52, 59]. This allows for the effects of hybridization (mixing of atomic orbitals) to be incorporated into the bonding energy during bond breaking and forming events [52, 59]. Advantages of this potential are that it incorporates mechanisms of covalent bonding into the descriptions of atomic interactions such as many-body effects and Coulomb interactions [52]. It also allows for the realistic modeling of the breaking and formation of atomic bonds that occur during a simulation. It can be used to model large systems of atoms for hundreds of picoseconds [52]. Disadvantages of this potential are that it does not explicitly treat electronic interactions and it is purely empirical [52], which means it needs to be fit to experimental or quantum mechanical data sets. However, the REBO potential is

still used for studying problems that are too computationally expensive for quantum mechanical methods [52].

2.3.2 The Lennard-Jones Interatomic Potential

The simplest realistic pair potential is the Lennard-Jones (LJ) 12-6 interatomic potential. J. E. Jones first developed this potential energy function in 1924 [66, 67]. The LJ potential describes the energy and force interactions between two neutral non-bonded atoms. The LJ potential is considered one of the simplest pair potentials because it is only a function of the atomic separation distance, ignoring angular or torsional effects, i.e.,

$$U_{ij} = 4\varepsilon \left[\left(\frac{\sigma}{r_{ij}} \right)^{12} - \left(\frac{\sigma}{r_{ij}} \right)^{6} \right]$$

<div align="right">Equation 2.13</div>

In Equation 2.10, r_{ij} is the separation distance between the ith and j[th] atoms. The parameter ε controls how strongly the two atoms interact with each other (the depth of the potential well). Therefore, if the value of ε is large (a deep potential well) then the atoms strongly interact. The parameter σ corresponds to the distance at which the potential energy between two atoms is zero (the point where the potential function crosses the horizontal axis). When the potential energy is equal to zero, $r = \sigma$. The values of ε and σ are specifically chosen to fit basic material properties [45].

The $1/r^{12}$ term describes the repulsive force between a pair of atoms and dominates the interaction at small distances, r. The origin of this term can be seen from the Pauli exclusion principle: as two atoms come closer together, their electron clouds begin to overlap and the energy of the system sharply increases making it an unstable state. The $1/r^6$ term describes the

attractive forces between a pair of atoms and dominates at large distances, r. The term models the weakly attractive dipole-dipole interactions that arise in neutral atoms from the electron-electron and electron-core interactions [45]. The LJ potential is most useful for modeling atoms with filled electron shells such as the noble gases. The LJ potential fails for atoms that have partially filled electron shells where strongly localized bonds can occur or the electrons are not localized as in metals [45]. The LJ potential is used very often in atomistic simulation to model electrostatic interactions between atoms that are fully coordinated by bonds within a molecule or crystal lattice, as will be done in this work between the S-Mo-S tri-layers.

2.4   Simulating Nanoindentation

Using a hard, nano-sized object to indent a crystal is one of the most popular methods for investigating the mechanical properties of materials. This technique provides information about the mechanical properties of materials by measuring the force exerted on an indenter tip as a function of the indenter displacement during indentation and retraction of the indentation tip [68, 69, 70]. With the development of sensitive experimental techniques such as the atomic force microscope, it is possible to measure the indenter displacement with nanometer accuracy [71]. With this nanoindentation technique, it is possible to create a force - displacement curves for a material. From these force - displacement curves, it is possible to determine the hardness of a material and the energies and forces required to create a defect or to initiate plastic flow [72, 73].

While nanoindentation experiments provide useful information about a material, it is difficult to infer what fundamental processes are occurring at the atomic level from this data in the initial stages of the experiment [69]. Atomistic simulations can be very helpful in studying the material response during nanoindentation because they are able to model discrete phenomena

and systems that are comparable to experimental sizes. The goal of atomistic nanoindentation simulations is to identify fundamental mechanisms in the early stages of deformation [74, 75]. These simulations, combined with visualization tools, allow atomic processes such as defect formation and plastic deformation to be connected with measurable macro-scale quantities [69, 74, 75].

Nanoindentation has become the focus of numerous atomistic studies of materials properties. For example, atomistic simulations of nanoindentation have been used to study: the nucleation and structure of defects in gold [72, 74], gold surface step effects on indentation load required for defect formation [70], the effects of indenter velocity on the hardness of nickel [68], dislocation nucleation, grain boundary structure and evolution and its effect on the plasticity of aluminum [76], the effect of the atomic structure on the hardness of amorphous silicon carbide [77], defect generation and pileup in single crystal iron [78], grain boundary effects and plasticity of nickel nanowires [79, 80], the effect of vacancies on defect nucleation in iron [73], and the mechanical properties of diamond, graphite, and fullerene thin films [81]. This list is not exhaustive but is used to demonstrate that the variety of uses and the increasing use of simulating nanoindentation.

In this work, a frictionless spherical indenter was used to model the nanoindentation process. This is an idealized indentation case where there are no attractive forces between the indenter and the atoms in the material being modeled, only repulsive forces [49, 72]. The repulsive force exerted by the indenter is given by:

$$F = -K(r_i - R)^2$$

Equation 2.14

In Equation 2.11, K is the force constant (effective stiffness) of the indenter, R is the radius of the indenter and r_i is the distance from the center of the indenter to the ith atom. During the simulation, if $r > R$ for a given atom, then the force felt by that atom due to the indenter was zero. If a given atom came into contact with the indenter during the simulation, $r \leq R$, then the atom felt a repulsive force given by Equation 2.14. The x, y, and z components of the force applied to all of the atoms contacting the indenter were determined and summed in each direction. This gave the total force experienced by the indenter tip in each direction, which was used to generate a force - displacement curve. The positions of the atoms are then updated to reflect the fact they had experienced an external force.

CHAPTER 3:   A PARAMETERIZED POTENTIAL FOR Mo-S SYSTEMS

This chapter provides an overview of the Liang *et al*. [28] interatomic potential that was parameterized for Mo-S systems and specifically for MoS_2 that was used in this work. Section 3.1 will provide a discussion of the reactive empirical bond-order (REBO) potential that has been parameterized to describe the covalent bonding that occurs within an S-Mo-S tri-layer. Section 3.2 provides a discussion of the modified Lennard-Jones 12-6 potential that was parameterized to describe the interlayer van der Waals interaction between the S-Mo-S tri-layers to study interlayer sliding and the tribological properties of MoS_2. With the Liang *et al*. [28] potential programmed into LAMMPS it was necessary to validate that the LAMMPS atomistic code that calculates the exact same values for energy and force quantities as the Liang *et al*. [28] atomistic code. Therefore, Section 3.3 will provide a description of the test cases and procedures used to compare energies and forces of the LAMMPS and Liang *et al*. [28] atomistic codes. With the LAMMPS atomistic code validated, a final test of its accuracy was to calculate lattice and elastic constants of body center cubic (BCC) molybdenum and MoS_2. Section 3.4 provides a discussion and the results of these calculations.

The Liang *et al*. [28] potential for Mo-S systems was implemented into LAMMPS for two main reasons. First, LAMMPS is a nationally maintained and open source classical molecular simulation tool. Second, LAMMPS has many more atomistic simulation features for studying materials. Some of the features of LAMMPS are: (i) it can model gaseous, liquid, or solid systems such as: polymers, biological or metallic structures, (ii) it was developed for efficient computing on single and multiple processors, (iii) it can model dozens to billions of atoms, (iv) the source code is designed to be easily modified to suite specific problems, (v) a large number of interatomic potentials are implemented to allow simulation of a variety of

materials and (vi) it has built in capabilities for studying mechanical properties of materials such as nanoindentation. A full list and description of the features of LAMMPS can be found at the LAMMPS website maintained by Sandia National Labs [49]. Therefore, incorporating the Liang *et al*. [28] potential into LAMMPS allowed for it to be distributed with the open source LAMMPS package so that it may be used and improved upon by other scientists and engineers that want to study this material with a very functional and highly maintained simulation tool with many capabilities.

3.1   The REBO Potential for Mo-S Systems

Liang *et al.* [28] modified and parameterized the REBO potential of Brenner *et al.* [59] to describe the covalent bonding that takes place within the S-Mo-S tri-layer. This Liang *et al.* [28] potential was fit to parameters of various prototype structures for pure molybdenum, pure and low coordinated sulfur and Mo-S to allow for transferability between Mo-S systems. Crystal properties such as bond length, energy per atom, energy per bond and bond stiffness were used in the fitting database for the REBO potential. These Mo, S and Mo-S properties were determined using quantum mechanical calculations. This potential was specifically parameterized to study MoS_2; therefore, not only was this potential fit to best reproduce the database of various structural properties, the properties of MoS_2 were given the largest weight during the fitting procedure by Liang *et al*. [28]. The database of structural properties for Mo, S, and Mo-S used during the fitting procedure of Liang *et al*. [28] can be found in Table 3.1.

Structures	Coordination number	Bond length (Å)	Energy per atom (eV)	Energy per bond (eV)	Bond stiffness (eV/Å^2)
Dimer	1	1.95	−6.41	−12.82	55.5[a]
Trimer	2	2.24	−6.53	−6.53	26.1[a]
Hexagonal	3	2.35	−7.78	−5.19	15.3
Square	4	2.47	−8.25	−4.13	12.4
Diamond	4	2.49	−8.61	−4.31	11.8
Triangle	6	2.61	−8.41	−2.80	6.9
sc	6	2.62	−9.58	−3.19	9.2
bcc[b]	8/14[c]	2.75[a](2.73[b])	−10.80[a]	−2.70[a]	8.0[a]
fcc	12	2.84	−10.38	−1.73	4.8

Table 3.1a: The fitting database for molybdenum structures [28].

Structures	Coordination number	Bond length (Å)	Energy per atom (eV)	Energy per bond (eV)	Bond stiffness (eV/Å^2)
Dimer	1	1.91	−3.28	−6.55	19.68
Trimer	2	2.03	−3.86	−3.86	11.56
Cyclo-octasulfur	2	2.04	−4.06	−4.06	11.42
Hexagonal	3	2.32	−3.30	−2.20	7.67
Square	4	2.38	−3.62	−1.81	5.63
Diamond	4	2.51	−3.13	−1.56	4.87
Triangle	6	2.54	−3.09	−1.03	3.50
sc	6	2.59	−3.51	−1.17	3.67
fcc	12	2.83	−2.84	−0.47	1.64
bcc	8	2.75[a]	−3.01[a]	−0.75[a]	2.35[a]

Table 3.1b: The fitting database for sulfur structures [28].

Structures	No. of bonds per unit	Bond length (Å)	Energy per unit (eV)	Energy per bond (eV)	Bond stiffness (eV/Å^2)
Cristo	4	2.23	−19.67	−4.92	16.22
Quartz	4	2.25	−19.72	−4.93	15.84
ZnS	4	2.32	−14.89	−3.72	13.97
TiO$_2$	6	2.41	−20.09	−3.35	11.63
MoS$_2$	6	2.44	−21.53	−3.60	13.16
NaCl	6	2.49	−14.47	−2.41	8.51
CaF$_2$	8	2.55	−19.47	−2.43	8.10
CsCl	8	2.62	−15.15	−1.89	6.25

Table 3.1c: The fitting database for Mo-S structures [28].

Following the analytic form of the second generation REBO potential of Brenner *et al.* [59], the Liang *et al.* [28] potential for Mo-S systems has the following form:

$$U = \sum_{i<j} f_{ij}^C(r_{ij})\left[V^R(r_{ij}) - b_{ij}V^A(r_{ij})\right]$$

$$= \sum_{i<j} f_{ij}^C(r_{ij})\left[\left(1 + \frac{Q_{ij}}{r_{ij}}\right)A_{ij}e^{-\alpha_{ij}r_{ij}} - b_{ij}B_{ij}e^{-\beta_{ij}r_{ij}}\right] \qquad \text{Equation 3.1}$$

In Equation 3.1, r_{ij} is the interatomic separation distance between the ith and jth atoms, $V^R(r_{ij})$ describes the repulsive interaction between atoms and $V^A(r_{ij})$ describes the attractive interactions between atoms. It should be noted that this attractive term is simpler than the attractive term given in Equation 2.9, as there is no summation. The function $f_{ij}^C(r_{ij})$ is the cutoff function that limits the REBO interactions to a maximum cutoff distance that only allows nearest neighbors to interact and b_{ij} is the many-body bond-order term. The parameters α_{ij}, β_{ij}, A_{ij}, and Q_{ij} are pairwise parameters that depend on the types atoms i and j that are interacting. The parameter Q_{ij} can be regarded as the screened Coulomb interaction [52]. These parameters are fit to reproduce specific material properties, which in this case are fit to reproduce lattice and elastic constants of MoS$_2$. In the following description of this potential, it will be seen that this REBO potential is in fact only a function of the atomic positions.

The cutoff function, $f_{ij}^C(r_{ij})$, only allows first and second nearest neighbor pairwise REBO interactions to occur within a defined range of distances (R_{ij}^{min} to R_{ij}^{max}) depending on what pairwise interaction is being considered. The cutoff function has been designed to gradually reduce the pairwise REBO interactions from a full interaction to a partial interaction to no interaction over the range R_{ij}^{min} to R_{ij}^{max}. The cutoff function is given by:

$$
f_{ij}^C(r_{ij}) = \begin{cases} 1 & r_{ij} < R_{ij}^{min} \\ \dfrac{1}{2}\left\{1 + \cos\left[\dfrac{\pi\left(r_{ij} - R_{ij}^{min}\right)}{\left[\left(R_{ij}^{max} - R_{ij}^{min}\right)\right]}\right]\right\} & R_{ij}^{min} < r_{ij} < R_{ij}^{max} \\ 0 & r_{ij} > R_{ij}^{max} \end{cases}
\qquad \text{Equation 3.2}
$$

To show that this function smoothly goes to zero to gradually reduce atomic interactions (energies and forces) over the range R_{ij}^{min} to R_{ij}^{max}, Figure 3.1 illustrates this function for Mo-Mo interactions.
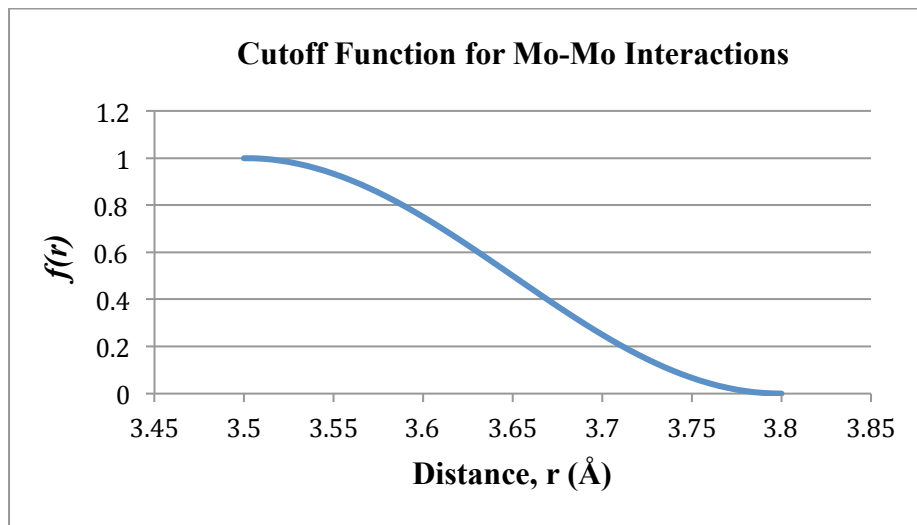
Figure 3.1: Graph of the Mo-Mo cutoff function illustrating the smooth decrease of the functions.

The bond-order term, b_{ij}, which can be viewed as the degree of bond strength, is determined by the many-body interactions of the local surroundings of atom i, such as any angular interactions and the coordination of atom i. The bond-order term rapidly decays as the coordination increases, which according to Abell is the dominant variable in determining the

bond-order [52]. In the Liang *et al.* [28] potential, the bond-order term has a similar form as Brenner *et al.* [59] and is given by,

$$b_{ij} = \frac{1}{2} \left[b_{ij}^{\sigma-\pi} + b_{ji}^{\sigma-\pi} \right]$$

Equation 3.3

Following the Brenner *et al.* [59] potential, the $b_{ij}^{\sigma-\pi}$ and $b_{ji}^{\sigma-\pi}$ terms are functions of bond angles and atomic coordination. As such they have a similar form and are given by (a similar form is given for $b_{ji}^{\sigma-\pi}$ by interchanging the i and j subscripts),

$$b_{ij}^{\sigma-\pi} = \left[1 + \sum_{k \neq i,j} f_{ik}^C(r_{ik}) G\left(\cos(\theta_{ijk})\right) + P(N_i) \right]^{-1/2}$$

Equation 3.4

The function, $f_{ik}^C(r_{ik})$, in Equation 3.4 is a cutoff function that limits the range of angular interactions that are considered. It has the same form as the cutoff function given in Equation 3.2. In Equation 3.3, the bond-order term is an average of $b_{ij}^{\sigma-\pi}$ and $b_{ji}^{\sigma-\pi}$ because of the use of Newton's Third Law in calculating atomic interactions. Therefore, given an atom i and a neighbor j, all angular interactions, θ_{ijk}, over all the neighbors, k, of atom i (with the exception of atom j) are considered as the summation in Equation 3.4 dictates. However, since Newton's Third Law is used, to properly average the bond-order terms, atoms i and j are interchanged and atom j is considered as the central atom. In this situation, all angular interactions, θ_{jik}, must be considered with the nearest neighbors, k, of atom j being considered as the angular interactions. This situation is illustrated in Figure 3.2. Note that in Figure 3.2 the neighbors of atom j are denoted as l to distinguish them from the neighbors of atom i.
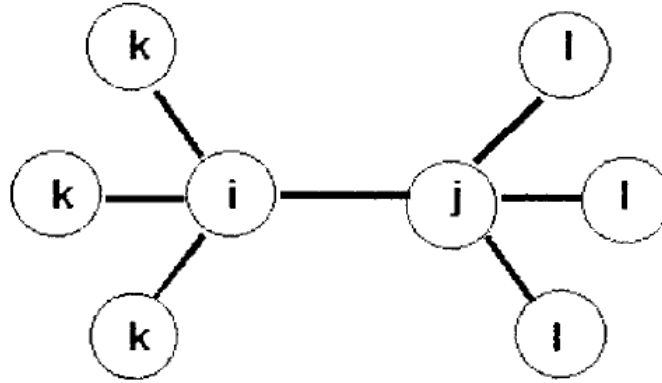
Figure 3.2: Illustration for determining angular interactions with nearest neighbors [52].

In Equation 3.4, the coordination function, which is the main variable in controlling the bond-order term, is represented by $P(N_i)$. $P(N_i)$ is a function of the coordination, N_i, (the total number of nearest neighbors within a given distance) of a given atom i. Therefore, as the coordination of an atom increases, the number of interactions increases and is therefore reflected in the value of the bond-order term, which will decrease and accordingly adjust the pairwise energy and force contributions. The function, $P(N_i)$, is given by,

$$P(N_i) = -a_0(N_i - 1) - a_1 e^{-a_2 N_i} + a_3 \qquad \text{Equation 3.5}$$

In Equation 3.5, the parameters a_i (i = 0, 1, 2, 3) are determined by the chemical species of the ith (or central) atom. These parameters are fit to reproduce bond-order values that will appropriately describe atomic energies and forces of given atomic configurations with increasing or decreasing coordination values. Figure 3.3 illustrates the response of the coordination function, $P(N_i)$, for Mo or S as a central atom.
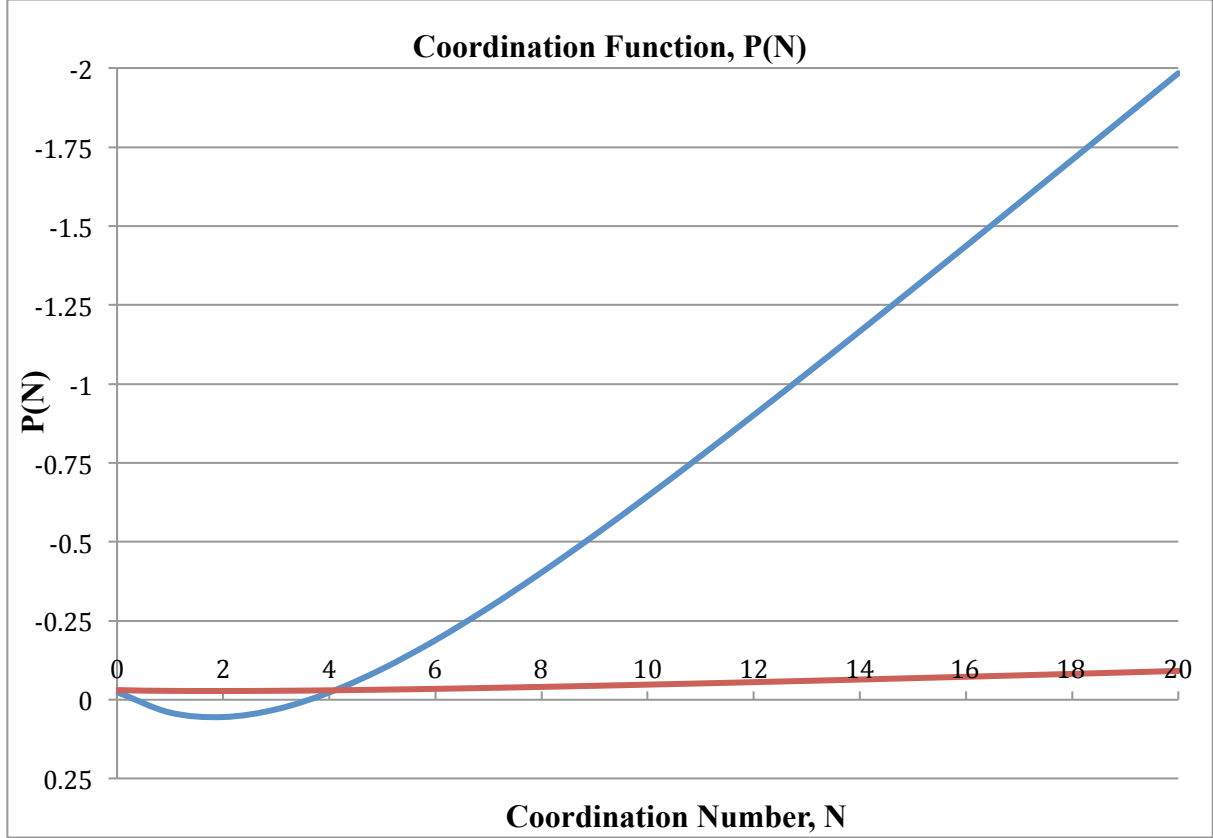
Figure 3.3: Coordination functions for Mo (Blue) and S (Red).

To describe energy and force contributions due to angular interactions from a set of atoms, an angular function is used and is represented as $G(\cos(\theta_{ijk}))$ in Equation 3.4. The function G depends on the cosine of the angle created by a set of atoms i, j and k. By using the Law of Cosines or the definition of the Dot Product, θ_{ijk} can be determined from the atomic positions. Therefore, the REBO potential as given in Equation 3.1 is solely a function of the atomic positions in the given system. The angular function, $G(\cos(\theta_{ijk}))$, is given by:

$$G[\cos(\theta_{ijk})] = G_0[\cos(\theta_{ijk})] + \psi[\cos(\theta_{ijk})]\{\gamma[\cos(\theta_{ijk})] - G_0[\cos(\theta_{ijk})]\} \qquad \text{Equation 3.6}$$

The functions $G_0[\cos(\theta_{ijk})]$ and $\gamma[\cos(\theta_{ijk})]$ shown in Equation 3.6 are given by sixth

order polynomials that are a function of the cosine of the angle created by a set of atoms i, j and

k and are written as:

$$G_0[\cos(\theta_{ijk})] = b_0 + b_1\cos(\theta_{ijk}) + b_2\cos(\theta_{ijk})^2 + b_3\cos(\theta_{ijk})^3 + b_4\cos(\theta_{ijk})^4$$
$$+ b_5\cos(\theta_{ijk})^5 + b_6\cos(\theta_{ijk})^6 \qquad \text{Equation 3.7a}$$

$$\gamma[\cos(\theta_{ijk})] = b_{g0} + b_{g1}\cos(\theta_{ijk}) + b_{g2}\cos(\theta_{ijk})^2 + b_{g3}\cos(\theta_{ijk})^3$$
$$+ b_{g4}\cos(\theta_{ijk})^4 + b_{g5}\cos(\theta_{ijk})^5 + b_{g6}\cos(\theta_{ijk})^6 \qquad \text{Equation 3.7b}$$

As with the a_i parameters in Equation 3.5, the parameters b_i and b_{gi} (i = 0 - 6) are fit to

produce appropriate bond-order values to describe atomic configurations to accurately reproduce

material properties. The function $G_0[\cos(\theta_{ijk})]$ in Equation 3.7a is used over the range

$0 \leq \cos(\theta_{ijk}) \leq \frac{1}{2}$. However, this function cannot be used over the range $\frac{1}{2} < \cos(\theta_{ijk}) \leq 1$

because this function creates a false energy well that causes atoms to become unrealistically

aligned. Therefore, the function $\gamma[\cos(\theta_{ijk})]$ is used in this region. The function $\psi[\cos(\theta_{ijk})]$ in

Equation 3.6 is used to provide a smooth transition from $G_0[\cos(\theta_{ijk})]$ to $\gamma[\cos(\theta_{ijk})]$ in this

region. Figure 3.4 illustrates the function $G_0[\cos(\theta_{ijk})]$ (Equation 3.7a) with its false energy wells

for Mo and S as well as $G[\cos(\theta_{ijk})]$ (Equation 3.6) which incorporates the additional function

$\gamma[\cos(\theta_{ijk})]$ (Equation 3.7b) to remove these energy wells. The function $\psi[\cos(\theta_{ijk})]$ is given by,

$$\psi[cos(\theta_{ijk})] = \begin{cases} 0 & , \cos(\theta_{ijk}) < \frac{1}{2} \\ \frac{1}{2}\left[1 - \cos\left(2\pi\left(\cos(\theta_{ijk}) - \frac{1}{2}\right)\right)\right], & \frac{1}{2} \leq \cos(\theta_{ijk}) \leq 1 \end{cases} \qquad \text{Equation 3.8}$$
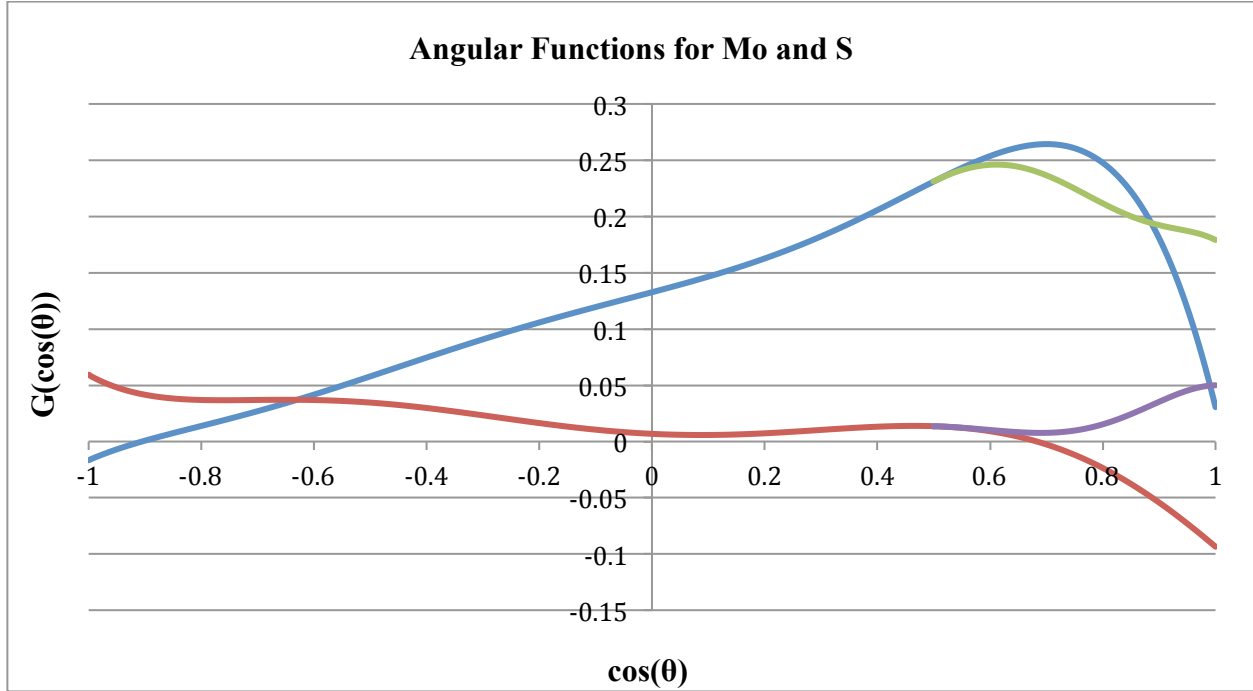
Figure 3.4: The angular functions for Mo and S (Blue = Mo, Red = S, Green = Mo Spline, Purple = S Spline).

All together, Equations 3.1 - 3.8 require 25 parameters for each unique interaction (Mo-Mo, S-S and Mo-S). The parameters used in this work for these interactions are listed in table 3.2.

Parameter	Mo-Mo	S-S	Mo-S
R^{min}	3.50	2.30	2.75
R^{max}	3.80	3.00	3.05
Q	3.41912939000591	0.254959104053671	1.50553783915379
A	179.008013654688	1228.43233679426	575.509677721866
α	1.0750071299934	1.10775022439715	1.1926790221882
B	706.247903589221	1498.64815404145	1344.46820036159
β	1.16100322369589	1.1267362361032	1.2697375220429

Table 3.2a: The pairwise parameters for the Mo-S REBO potential used in this work.

Parameter	Mo	S
b_0	0.132684255066327	0.00684876159675
b_1	-0.007642788338017	-0.02389964401024
b_2	0.034139577505937	0.13745735331117
b_3	0.252305097138087	0.03301646749774
b_4	0.122728737222567	-0.3106429154485
b_5	-0.361387798398897	-0.08550273135791
b_6	-0.282577591351457	0.14925279030688
b_{g0}	0.12019430103528	-0.2850852
b_{g1}	0.04523828735819	1.6710248
b_{g2}	0.06792280724403	-3.5678516
b_{g3}	-0.03672511378682	3.4505499
b_{g4}	0.10751647751386	-1.2186289
b_{g5}	0.00496471198494	0.0
b_{g6}	-0.12997598358652	0.0
a_0	0.138040769883614	0.062978539843324
a_1	0.803625443023934	2.47861761987825
a_2	0.292412960851064	0.036666243238154
a_3	0.640588078946224	2.38643137248671

Table 3.2b: The many-body parameters for the Mo-S REBO potential used in this work.

3.2 The Lennard-Jones Potential for Mo-S Systems

Not only was the REBO potential parameterized for Mo-S systems, but the Lennard-Jones 12-6 potential described in Section 2.3 was also parameterized for Mo-Mo, S-S and Mo-S interactions. The Lennard-Jones potential was parameterized to describe the van der Waals interaction between the S-Mo-S tri-layers. This allows for the frictional properties of MoS_2 to be accurately investigated. In the Liang *et al.* [28] atomistic code, the Lennard-Jones potential was separated into two regions. Region I is defined as $0.95\sigma_{ij} \leq r_{ij} \leq R_{ij}^{max}$ while region II is defined as $R_{ij}^{min} \leq r_{ij} < 0.95\sigma_{ij}$. Here r_{ij} is the atomic separation distance, R_{ij}^{min} and R_{ij}^{max} are the minimum and maximum cutoff distances for pairwise interactions as defined by the REBO potential and σ_{ij} is the corresponding Lennard-Jones pairwise parameter determined by the chemical species of atoms i and j. When the atomic separation distance is within region I, the

atomic interactions are described by the Lennard-Jones potential as given in Equation 2.13. However, at small atomic separation distances, the Lennard-Jones potential has an unrealistic repulsive wall with corresponding large repulsive forces. Therefore, when atomic separation distances fall within region II, a spline is used to describe the atomic interactions and at the same time to remove this unrealistic repulsive wall. This spline is designed to smoothly terminate the Lennard-Jones interactions at R_{ij}^{min}. The use of this spline allows for a better description of the interlayer interactions of MoS$_2$. The spline used to describe the Lennard-Jones interactions within region II has the following expression,

$$
U_{LJ}^S(r_{ij}) = \frac{(r_{ij} - R_{ij}^{min})^2}{(0.95\sigma_{ij} - R_{ij}^{min})} \left\{ (r_{ij} - R_{ij}^{min}) \left[\frac{-2E_{LJ}(0.95\sigma_{ij})}{(0.95\sigma_{ij} - R_{ij}^{min})^2} + \frac{\partial E_{LJ}(0.95\sigma_{ij})}{(0.95\sigma_{ij} - R_{ij}^{min})} \right] \right.
$$
$$
\left. + \left(\frac{3E_{LJ}(0.95\sigma_{ij})}{(0.95\sigma_{ij} - R_{ij}^{min})} - \partial E_{LJ}(0.95\sigma_{ij}) \right) \right\} \qquad \text{Equation 3.9}
$$

In Equation 3.9, r_{ij} is the atomic separation distance, R_{ij}^{min} is the minimum REBO cutoff distance, σ_{ij} is the Lennard-Jones parameter for the i –j interaction as determined by their atom types, $E_{LJ}(0.95\sigma_{ij})$ is the normal Lennard-Jones potential (Equation 2.13) evaluated at the location $0.95\sigma_{ij}$ and $\partial E_{LJ}(0.95\sigma_{ij})$ is the derivative of the Lennard-Jones potential (Equation 2.13) evaluated at the location $0.95\sigma_{ij}$. To illustrate the Lennard-Jones potential as a function of atomic separation distance, Figure 3.5 provides a graph of the Lennard-Jones potential and spline for S-S interactions for regions I and II.
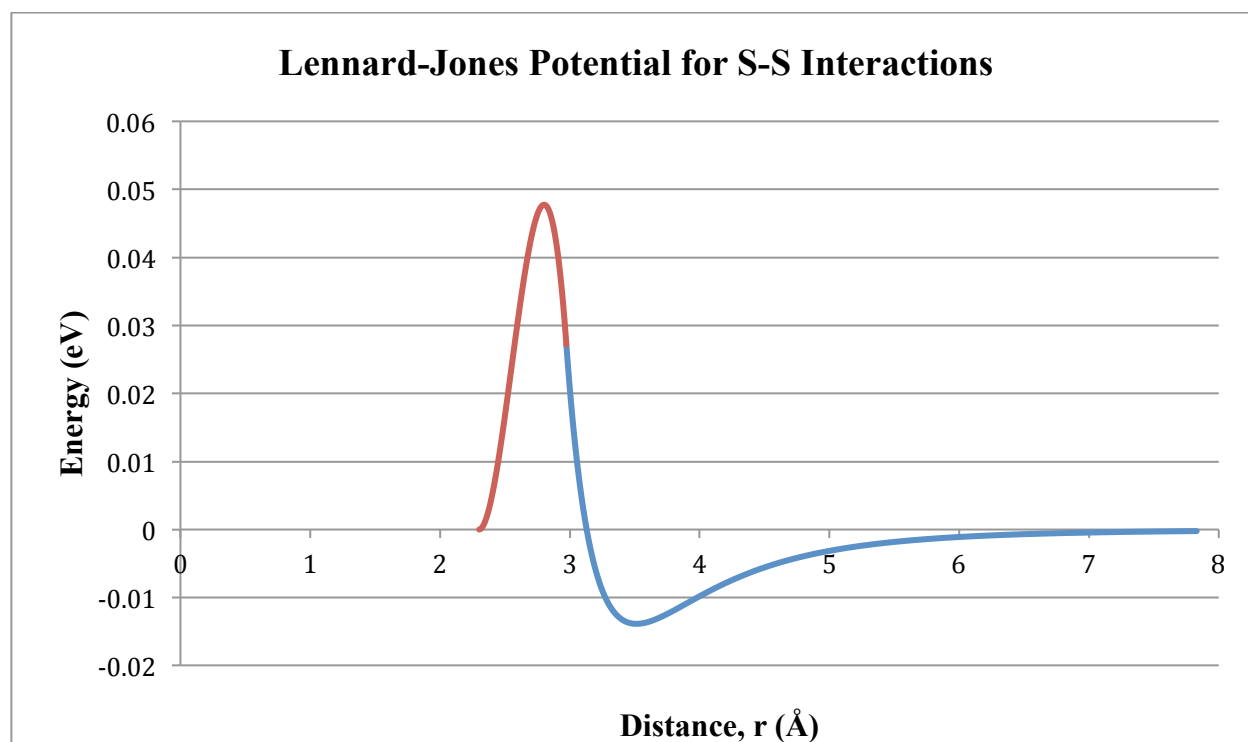
Figure 3.5: Lennard-Jones potential for S-S interactions (L-J Spline = Red, L-J Potential = Blue).

The Lennard-Jones parameters used in this work for Mo-Mo, S-S and Mo-S interactions are listed in Table 3.3. It should be noted that the Lennard-Jones parameter ε used by LAMMPS in this work for S-S interactions is different than the value of ε used by Liang *et al.* [28]. The value of ε for S-S interactions was chosen to best reproduce the value of C_{33} for MoS$_2$. However, Liang *et al.* [28] calculated elastic constants for MoS$_2$ at with their simulation equilibrated to 300 K. The method of calculating elastic constants in the LAMMPS package is done with the system at 0 K. This temperature difference in determining an appropriate value of ε will cause different elastic constants to be calculated. Therefore, a new value of ε for S-S interactions will be needed for the LAMMPS implementation and this work to accurately model the interlayer van der Waals interactions during energy minimization, i.e., at 0 K. As such, a value of ε was chosen to best

reproduce the elastic constants of MoS_2 as determined by the DFT work carried out by Weber *et al.* [34], as discussed in Section 1.2. The elastic constants and the method for calculating them will be discussed in Section 3.4.

Parameter	Mo-Mo	S-S	Mo-S
ε (eV)	0.00058595	0.01386	0.0028
σ (Å)	4.2	3.13	3.665

Table 3.3: The pairwise parameters for the Lennard-Jones potential used in this work.

3.3 Validation of the Implemented LAMMPS Mo-S Potential

With Equations 3.1 - 3.9 programmed into LAMMPS, it was necessary to validate that this implementation accurately reproduced these equations and matched the Liang *et al.* [28] atomistic code. In order to validate that these codes produced the same result, each quantity associated with Equations 3.1 - 3.9 were directly compared between the LAMMPS and Liang *et al.* [28] codes. To compare these quantities, special three-atom test cases with a known geometry was chosen as shown in Figure 3.6.
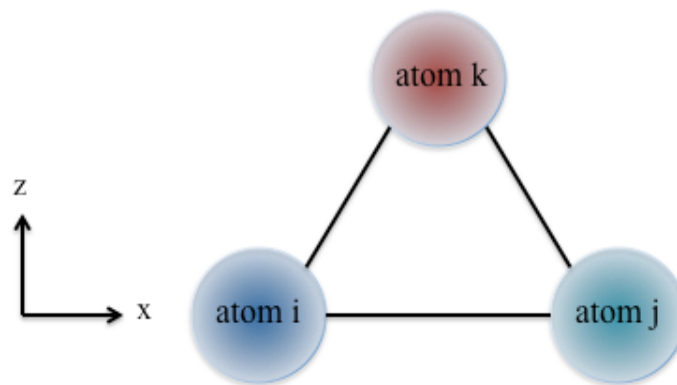
Figure 3.6: Three-atom test geometry for LAMMPS validation with corresponding Cartesian axis.

This three-atom case was chosen because it is simple and the quantities calculated with Equation 3.1 - 3.8 could easily be compared. Also, the three-atom system was situated in such a way that the force components were known to be zero in certain directions. In Figure 3.6, the atoms i, j and k were located in the x-z plane. Three sets of comparisons were done with this geometry using different atom types. The first calculation compared this three-atom geometry with three molybdenum atoms, the second calculation compared three sulfur atoms, and the third calculation compared one molybdenum atom and two sulfur atoms. Using this configuration and Equations 3.1 - 3.9, the energy per atom and the individual quantities comprising Equations 3.1 - 3.9 were calculated using the Liang *et al.* [28] and LAMMPS atomistic codes. Using this procedure it was verified that the LAMMPS implementation accurately reproduced the energies and energy quantities associated with Equation 3.1 - 3.9 that the Liang *et al.* [28] code calculated. With both codes verified to calculate the same energetics of a given system, next it was necessary to compare the force calculations associated with Equations 3.1 - 3.9 (the derivatives of these expressions shown in Appendix H) to ensure that the LAMMPS implementation produced the same atomic forces and mechanical properties as predicted with the Liang *et al.* [28] code. Using the same three-atom configuration in Figure 3.6 and the same procedure as with the energy validation, the x, y and z components of the atomic forces were compared. Using the three atom configuration in Figure 3.6 and comparing the energy and force calculations for the Liang *et al.* [28] and LAMMPS atomistic codes, it was determined that the Liang *et al.* [28] potential that was parameterized for Mo-S systems was properly programmed into the LAMMPS simulation package.

3.4   Structural and Elastic Properties of BCC Molybdenum and MoS$_2$

Once it was determined that the LAMMPS implementation of the Liang *et al.* [28] Mo-S

potential was properly programmed and calculating correct atomistic quantities, it was necessary

to calculate the structural and elastic properties of the main structures that Liang *et al.* [28] used

to parameterize their potential; mainly body centered (BCC) molybdenum and crystalline MoS$_2$.

It should first be noted that Liang *et al.* [28] used a different method to calculate these quantities

than is done in this work with the LAMMPS implementation. Therefore, minor differences were

expected to arise in the resulting values of these quantities. In calculating the lattice and elastic

constants, Liang *et al.* [28] first applied a strain of +/- 1% from the known equilibrium bond

lengths to their simulation cell. They then equilibrated the simulation cell, with the applied

strain, to a temperature of 300 K. With the simulation cell at 300 K, the simulation was run for a

period of time, during which the energy of the system was recorded at each time step. Using this

energy information, the average energy of the system during the simulation run was then

computed. With the average energy of the simulation crystals known at 0% strain and +/- 1%

strain, a quadratic equation was then fit to this data as a function of bond length, r, i.e.,

$$E(\text{r}) = \ c_0 + c_1\text{r} + c_2\text{r}^2$$

Equation 3.10

In Equation 3.10, c_0, c_1 and c_2 are constants from fitting the quadratic polynomial to the

energies of the strained and unstrained structures. Using Equation 3.10, Liang *et al.* [28]

calculated the equilibrium lattice constants and the elastic constants, which are related to the

second derivative of Equation 3.10, for BCC molybdenum and crystalline MoS$_2$ at 300 K.

To calculate the lattice and elastic constants for BCC molybdenum and MoS_2 using LAMMPS, an energy minimization (Section 2.2) procedure was used. Using energy minimization means that the lattice and elastic constants were computed at 0 K. To calculate the lattice constants, energy minimization was done to ensure the structures were in their minimum potential energy state. Once the energy of the structures was minimized, the distances between atoms corresponding to the lattice parameters for BCC molybdenum (a) and MoS_2 (a and c) as well as the energy per atom for BCC molybdenum and energy per unit for MoS_2 were calculated. To calculate the elastic constants for BCC molybdenum and MoS_2, a strain of +/- 1% was applied to the simulation cells. The elastic constants C_{11} and C_{12} were calculated for BCC molybdenum and the elastic constants C_{11} and C_{33} were calculated for MoS_2. Figure 3.7 shows the MoS_2 structure with the corresponding Cartesian axes that define the directions that the strain was applied.
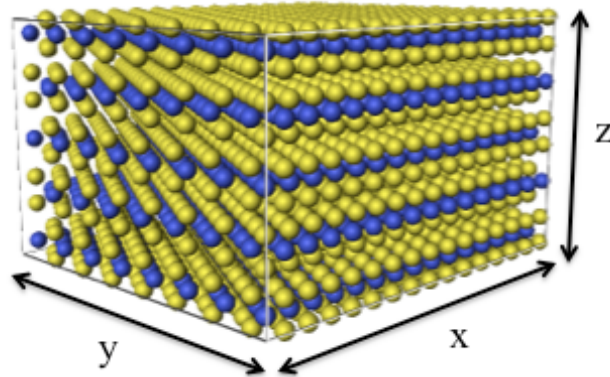
Figure 3.7: MoS_2 structure and corresponding Cartesian axes.

For BCC molybdenum, to calculate C11 the simulation cell was expanded and compressed by 1% in the x-direction, while the box was expanded by 1% in the x-y direction (the simulation cell diagonal) to calculate C_{12}. Similarly for MoS_2, the simulation cell was

expanded and compressed by 1% in the x and z directions to calculate C_{11} and C_{33} respectively.
By calculating the pressures (equivalently the stresses) of the initial, compressed and expanded
crystal configurations it was then possible to determine the elastic constants C_{11}, C_{12} and C_{33}. To
calculate these constants, the following equations [49, 82] were used:

$$\frac{\partial U_0}{\partial \varepsilon_{xx}} = C_{11}\varepsilon_{xx} \qquad\qquad \text{Equation 3.10a}$$

$$\frac{\partial U_0}{\partial \varepsilon_{xy}} = C_{12}\varepsilon_{xy} \qquad\qquad \text{Equation 3.10b}$$

$$\frac{\partial U_0}{\partial \varepsilon_{zz}} = C_{33}\varepsilon_{zz} \qquad\qquad \text{Equation 3.10c}$$

In Equation 3.10, the variable ε is the strain applied to the simulation cell in a
corresponding direction as given by the subscripts, assuming zero strain in all other directions.
The quantity $\partial U_0/\partial \varepsilon$ defines the change in the pressure (or stress) of the crystal in the direction
the strain is applied. The lattice and elastic constants for BCC molybdenum and crystalline MoS_2
as determined by the methods described above for Liang *et al.* [28] and this work are compared
in Table 3.4.

BCC Molybdenum	Liang *et al.* [28]	This Work
Energy per Atom (eV)	-10.38*	-10.77
a (Å)	3.16	3.16
C_{11} (GPa)	319	319.9
C_{12} (GPa)	214	220.5
Bulk Modules (GPa)	249	253.6

Table 3.4a: Lattice and elastic constants for BCC molybdenum from Liang *et al.* [28] and this
work (* denotes DFT calculation used in the Liang *et al.* [28] fitting procedure).

MoS$_2$	Liang *et al.* [28]	This Work
Energy per Unit (eV)	-21.23*	-21.59
a (Å)	3.15	3.17
c (Å)	12.26	12.29
C$_{11}$ (GPa)	222	255.24
C$_{33}$ (GPa)	23	36.99

Table 3.4b: Lattice and elastic constants for MoS$_2$ from Liang *et al.* [28] and this work (* denotes DFT calculation used in the Liang *et al.* [28] fitting procedure).

3.5   Summary

In summary, a parameterized reactive empirical bond-order (REBO) potential that has been parameterized by Liang *et al.* [28] has been incorporated into the LAMMPS molecular simulation package. The LAMMPS implementation was tested on small three atom test cases to verify that it was mathematically equivalent to the Liang *et al.* [28] atomistic code and calculated the same values for corresponding energy and force quantities. Additionally, the lattice and elastic constants of BCC molybdenum and crystalline MoS$_2$ were calculated in this work using LAMMPS and compared to the lattice and elastic constants as determined by Liang *et al.* [28] to determine the ability of the parameterized Mo-S potential to model MoS$_2$. With this Mo-S potential properly programmed into LAMMP, this potential was used to model crystalline MoS$_2$ during nanoindentation simulations discussed in Chapter 4.

CHAPTER 4: NANOINDENTATION OF CRYSTALLINE MoS$_2$

This chapter provides simulation results of nanoindentation on the MoS$_2$ basal plane (the plane perpendicular to the c-axis) using the Liang *et al*. [28] Mo-S potential. Section 4.1 provides a brief discussion of Hertzian contact theory [83], which is widely used in atomistic simulations of nanoindentation. Section 4.2 provides the nanoindentation simulation procedures used in this work. Section 4.3 discusses the elastic response of MoS$_2$ during nanoindentation and the resulting initial plastic event. Section 4.4 discusses the deformation mechanisms associated with the initial plastic event. Finally, Section 4.5 discusses the effect of the indenter size on the stresses and depths required for failure.

4.1   Nanoindentation Simulation Background

Nanoindentation experiments and simulations can provide information about the mechanical properties of materials at the nanometer and atomic length scales. Atomistic simulations of nanoindentation allow for easy identification and visualization of defects, defect nucleation and defect structure with the aide of visualization tools [75]. In nanoindentation simulations, an indenter, which can be perfectly spherical (as was used in this work) or modeled using atoms with different shapes such as a pyramidal indenter, is pushed into a simulated infinite film of material. The displacement of the indenter is controlled during the simulations, and the indenter force is computed at each indenter displacement. This allows the determination of the force required for a material to plastically deform. During displacement-controlled indentation simulations, a sudden drop in the indenter load identifies plastic deformation of a material. The sudden drop in the indenter force (or point plastic deformation) is a consequence of

the nucleation of defects or a phase transition [75]. With the indenter displacement and indenter force at each displacement position, a force-displacement curve can be generated to study the elastic and plastic responses of the material. The ideal elastic deformation regime of contacting materials (resulting force as a function of displacement) is predicted by the Hertzian contact theory. Therefore, the elastic response of a material as determined by a simulation can be compared to the predictions of Hertzian contact.

In Hertzian contact theory [68, 72, 74, 83], for a spherical indenter contacting an infinite slab of elastic material the indenter load can be related to the displacement of the indenter. The indenter force, F, is related to the displacement, d, of the indenter by:

$$F = \frac{4}{3} E^* R^{1/2} d^{3/2} \qquad \text{Equation 4.1}$$

where R is the radius of the indenter and E^* is the reduced modulus of the system (indenter and sample). The reduced modulus is a function of the elastic moduli of the indenter, E_i, and sample, E_s, as well as the Poisson ratios for the indenter, ν_i, and sample, ν_s, and is determined by

$$\frac{1}{E^*} = \frac{1 + \nu_s^2}{E_s} + \frac{1 + \nu_i^2}{E_i} \qquad \text{Equation 4.2}$$

Recall that the elastic modulus is a measure of the stiffness of a material and Poisson's ratio is a measure of how much a material will contract laterally when a tensile force is applied the material and depends on the axial and perpendicular strains [84]. Equation 4.2 expresses the

reduced modulus for an indenter and sample that are both elastic. With a perfectly rigid indenter the reduced modulus becomes a function of the sample only i.e.,

$$\frac{1}{E^*} = \frac{1 + v_s^2}{E_s} \qquad \text{Equation 4.3}$$

As the indenter is displaced further into the material, the contact area, A_C, between the indenter and sample increases and is determined by [68]

$$A_C = \pi(2Rd - d^2) \qquad \text{Equation 4.4}$$

Using Equations 4.1 and 4.4, it is also possible to calculate the mean contact pressure experienced at each displacement depth of the indenter. The mean contact pressure is equivalent to the indentation hardness, H, and is defined in experiments to be $H = P_C = F/A_c$ [68, 74].

The Hertzian contact model describes the elastic response of a material. When the indenter load drops suddenly due to the formation of defects, the Hertzian description is no longer valid. In nanoindentation simulations, the Hertzian contact description is generally used to compare against the force-displacement data generated during the simulation for the elastic regime. For example, Lilleodden *et al.* [74] studied the initial stages of nanoindentation on (111) Au and (001) Au using the embedded atom method (EAM) potential, an indenter of radius of 40 Å and force constant, K, of 10 eV/Å^3. The indenter force-displacement graph generated by this nanoindentation simulation is shown in Figure 4.1a. The black dots and circles represent the force-displacement data for (111) Au and (001) Au respectively. The solid and dashed lines represent the best fit of Equation 4.1 (the Hertzian description) to these (111) Au and (001) Au force-displacement indentation responses respectively.
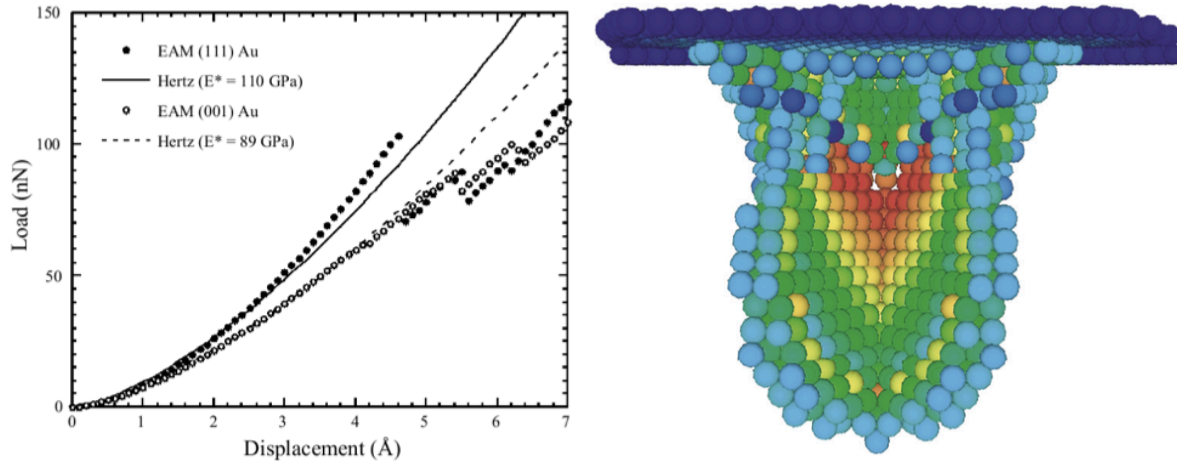
Figure 4.1: (a) Load-displacement curves for nanoindentation of (111) Au and (001) Au [74] (b) Partial dislocations associated with the load drop in (111) Au nanoindentation [74].

From Figure 4.1a, it is clear that there is a sudden drop in the indenter load at 4.6 Å for (110) Au and 5.4 Å for (001) Au, which corresponds to the formation of a defect. From the best-fit curves in Figure 4.1a, Lilleodden *et al*. [74] calculated a reduced modulus of 110 GPa for (111) Au and 89 GPa for (001) Au. It was also calculated that the pressure of the (111) Au system was 18 GPa before the indenter load dropped.

To investigate the mechanism associated with the formation of a defect, Lilleodden *et al*. [74] used a combination of the centro-symmetry parameter and the slip vector along with the force-displacement nanoindentation data. The centro-symmetry parameter is a quantity that provides a measure of the local disorder around an atom in a BCC or FCC structure. It can be used to determine if an atom is in a perfect lattice, near a defect (dislocation or stacking fault) or at a surface location [49, 72, 74]. The slip vector is a measure of the displacement of atoms from their original positions relative to their nearest neighbors [70, 74]. The slip vector is used to determine the Burgers vector (a vector defining the magnitude and direction of lattice distortion) of a dislocation created from nanoindentation so that elastic and plastic strains can be separated

and the slip direction can be determined [70, 74]. The defects produced by Lilleodden *et al.* [74] for (111) Au indentation are shown in Figure 4.1b and correspond to the sudden load drop in Figure 4.1a. The partial dislocations shown in Figure 4.1b were characterized by a slip-vector analysis and the associated atoms were colored according to their centro-symmetry parameter [74]. The light blue and yellow atoms correspond to the leading and trailing edges of the defect; the green atoms correspond to a stacking fault being created and the red atoms denote the region of space where the dislocation has fully passed through and left behind a perfect lattice with atoms that have moved a full lattice vector [74].

It should be noted that MoS_2 doesn't have the required constraints to allow the use of traditional defect nucleation analysis tools such as the centro-symmetry parameter, which requires every point in the system to have inversion symmetry [49, 72, 74], or common neighbor analysis, which works only with materials that contain a single atomic species [49]. As such, it was necessary to investigate crystal disorder by a different method. In this work, this was done mainly by explicitly analyzing the atomic bonding of nearest neighbors to determine the existence of broken bonds. Doing this allowed the sudden drop in indenter force to be correlated to the creation of broken bonds or indicate another type of deformation mechanism.

4.2 Nanoindentation Simulation Procedure

In order to study defect nucleation in MoS_2 during nanoindentation, a single crystal film of MoS_2 was created with dimensions of 500 Å x 500 Å x 227 Å and consisting of 3,267,840 atoms (Figure 4.2). Periodic boundary conditions were applied in the x and y direction while the basal plane (z direction) was represented by a free surface. The large size of this simulation cell was chosen to remove any effects of the finite size of the simulation on the nanoindentation

results. The bottom layer of atoms was defined to be fixed (rigid) to provide a stable nanoindentation substrate [68, 74]. To simulate nanoindentation of MoS_2, a rigid spherical indenter (as described in section 2.4) was used [72]. To study defect nucleation and deformation (the initial plastic event) of MoS_2, indenter sizes of 50 Å, 75Å and 100 Å were used. The force constant for all indenter sizes was taken to be 10 eV/Å^3 [72, 74]. Before the nanoindentation process, the MoS_2 crystal was energetically relaxed using the energy minimization procedure described in Section 2.2. During the nanoindentation process, the indenters were moved in 0.2 Å increments. After each indenter displacement, the energy of the system was minimized and the resulting force experienced by the indenter was determined [72, 74]. Visualization of these nanoindentation simulations was done with OVITO (The Open Visualization Tool) [85].
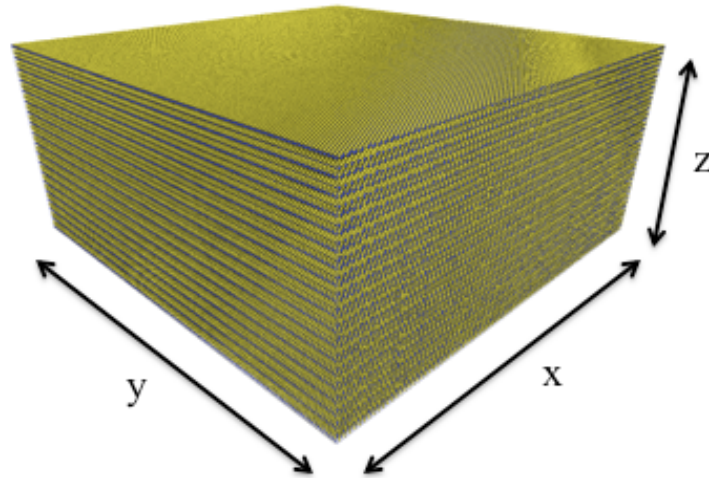
Figure 4.2: Illustration of the MoS_2 crystal slab used in the nanoindentation simulations (Sulfur = Yellow, Molybdenum = Blue).

4.3   Nanoindentation of the MoS₂ Basal Plane

To investigate the mechanisms associated with defect nucleation and plastic deformation due to nanoindentation, it was necessary to displace the three indenters into the MoS$_2$ simulation crystal to ensure that elastic and plastic events occurred and were captured. This was done by displacing the three indenters to a depth of 10 Å (1 nm) during the simulation. In doing this, three relatively large and sudden drops in the indenter force occurred for each of the indenters. The resulting force-displacement curves for these three indenter sizes are shown in Figure 4.3. The focus of this work was the initial deformation event due to this nanoindentation. Therefore, the first sudden force drop region, which occurs at 1.8 Å for the 50 Å indenter and 1.6 Å for the 75 Å and 100 Å indenters, is the region of interest for investigating the initial defect and/or deformation formation.
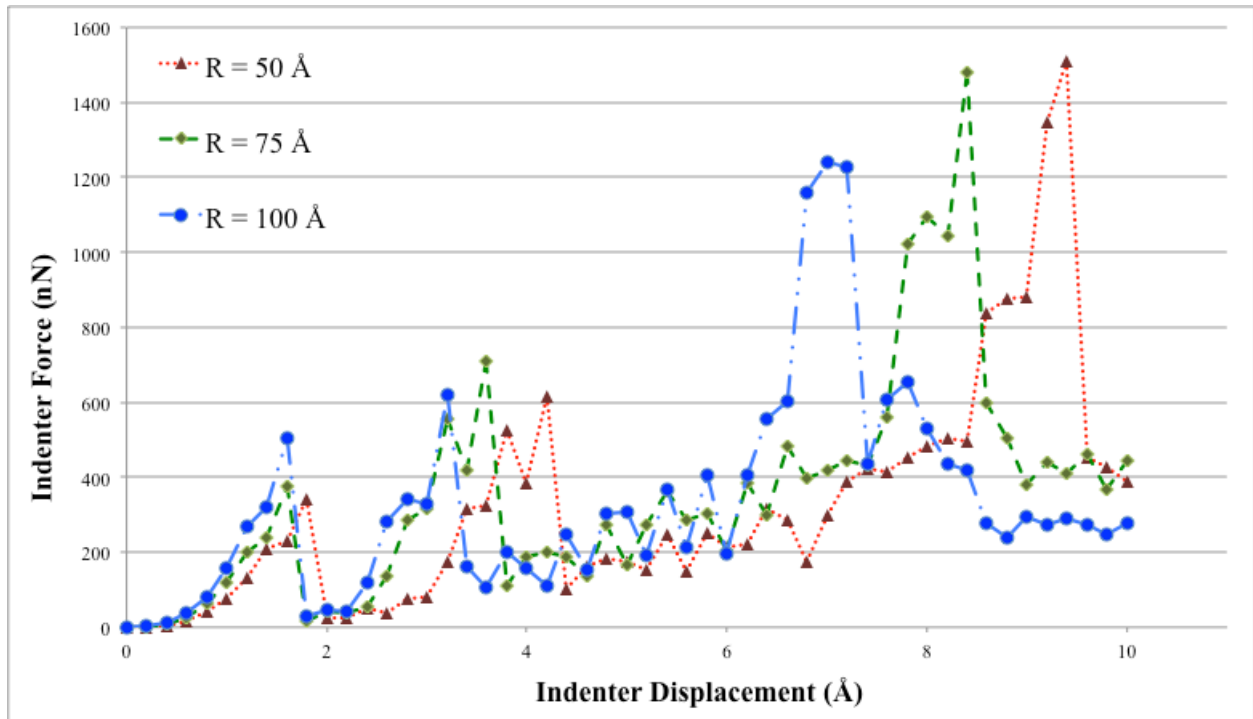
Figure 4.3: The force - displacement curves for nanoindentation of MoS$_2$ with 50, 75 and 100 Å indenters to a displacement depth of 10 Å. (The dotted lines show trend of data and not physical quantities).

To verify that these initial sudden force drops were associated with permanent plastic failure events, indentation and retraction simulations were performed. Once the indenters were displaced to the depths corresponding to the sudden force drops, they were retracted and the indenter force was calculated at each displacement. It was found that as the indenters were retracted, the indenter force quickly dropped to zero. This meant that the indenter was no longer in contact with the MoS_2 crystal, which meant that the MoS_2 crystal did not recover from the deformation. Therefore, the deformation associated with these sudden force drops corresponded to permanent deformation that was energetically stable. The force - displacement curves for the indentation and retraction simulations are shown in Figure 4.4. Also shown in Figure 4.4 are minor force events at displacements of 1.2 Å and 1.4 Å. These events corresponded to elastic movement of atoms below the indenter. This was determined by indenting and retracting to these displacements. As the indenters were retracted, the force on the indenter at each displacement was the same as the corresponding indentation displacement force.
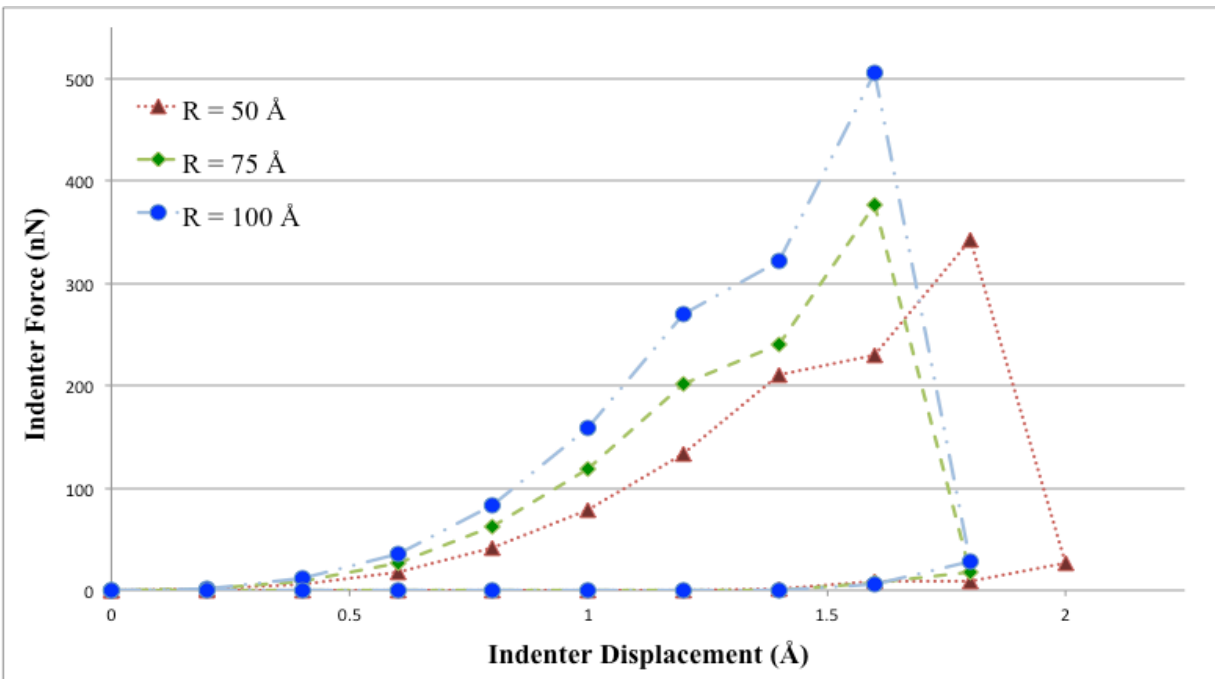
Figure 4.4: The force - displacement curves for indentation and retraction of MoS_2 with 50, 75 and 100 Å indenters. (The dotted lines show trend of data and not physical quantities).

62

With the elastic and initial plastic regions determined, the elastic response of MoS_2 during nanoindentation was then compared to the Hertzian description (Equation 4.1) of elastic material response. The best fit of the Hertzian description to the force - displacement data during indentation to the displacement depths right before the sudden force drop are shown in Figure 4.5. The solid lines represent the best fit of the Hertzian description. By substituting the indenter radius into the best-fit curves of the force - displacement profiles, it was possible to calculate effective reduced moduli (Equation 4.3) for each indenter size. The effective reduced moduli for each indenter were found to be 12.6 GPa for the 50 Å indenter, 13.4 GPa for the 75 Å indenter and 15.6 GPa for the 100 Å indenter. It is important to note that the Hertzian contact description assumes isotropic elastic behavior of the indented material. However, MoS_2 is not an isotropic material but rather highly anisotropic (recall the MoS_2 elastic constants: C_{11} = 255.24 GPa and C_{33} = 36.99 GPa). Therefore, these reduced moduli are not directly relevant to the physical properties of MoS_2. However, these reduced moduli reflect the fact that MoS_2 is a soft material in the direction of nanoindentation.
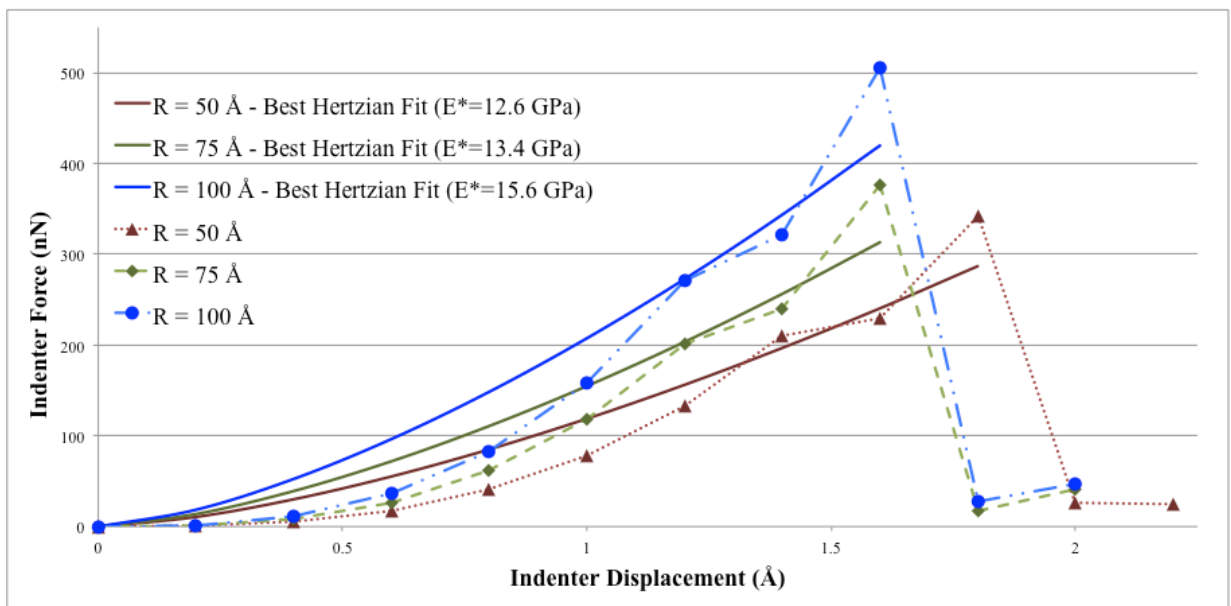
Figure 4.5: The force-displacement curves for the 50, 75 and 100 Å indenters with the best-fit Hertzian prediction curves. (The dotted lines show trend of data and not physical quantities).

63

Also shown in Figure 4.5 is that, for small indenter displacements, the force - displacement curve exhibits smooth elastic behavior. However, as expected and indicated above, these results did not follow the Hertzian relation within the elastic response regime. This was attributed to the fact that MoS_2 is a layered and highly anisotropic material. Therefore, as the indenter is displaced into the MoS_2 film, the layers compress since there is only a weak van der Waals interaction between layers and the resulting indenter force would be lower than would be predicted in the Hertzian contact theory. Initially the planar S-S distance within the top MoS_2 layer is 3.214 Å while the planar S-S distance between the top two MoS_2 layers is 2.9 Å. At the point right before the sudden force drop, the top MoS_2 layer had compressed to a new S-S planar distance of 2.99 Å and the planar S-S distance between the top two MoS_2 layers had compressed to a distance of 2.89 Å. As the MoS_2 layers compress closer together the atomic repulsion forces increase and prevent further compression of the layers and as a result the indenter force starts to quickly increase until failure occurs. In addition, using Equation 4.4, the maximum contact pressure is approximated to be 0.62 GPa, 0.51 GPa and 0.51 GPa for the 50 Å, 75 Å and 100 Å indenters, respectively, at the indenter displacement immediately before plastic yield.

Visualization of these atomistic simulations allows for explicit observation of the atomic configurations during the simulation as well as the forces experienced by each atom within the system or any physical quantity that can be calculated. In this work, OVITO [85] (The Open Visualization Tool) was used to visualize the nanoindentation simulations. OVITO was used to visualize the atomic configurations and force magnitude on each atom located under the indenter tip immediately before and immediately after the sudden drop in the indenter force. Figure 4.6 illustrates the atomic configurations and the magnitude of the force on each atom before the first drop in force for the nanoindentation simulation with the 50 Å indenter, while Figure 4.7

illustrates the atomic configuration and the magnitude of the force on each atom after the first force drop event. It is clearly seen in these images and the corresponding inlayed force - displacement curves that when the indenter force suddenly drops, the force that had built up on the atoms located directly under the indenter has dissipated and its position has moved to within the MoS_2 crystal, which is an indication of permanent deformation within the MoS_2 lattice. Also shown in Figure 4.7 is that the MoS_2 layers have bent as a result of the force dissipation.
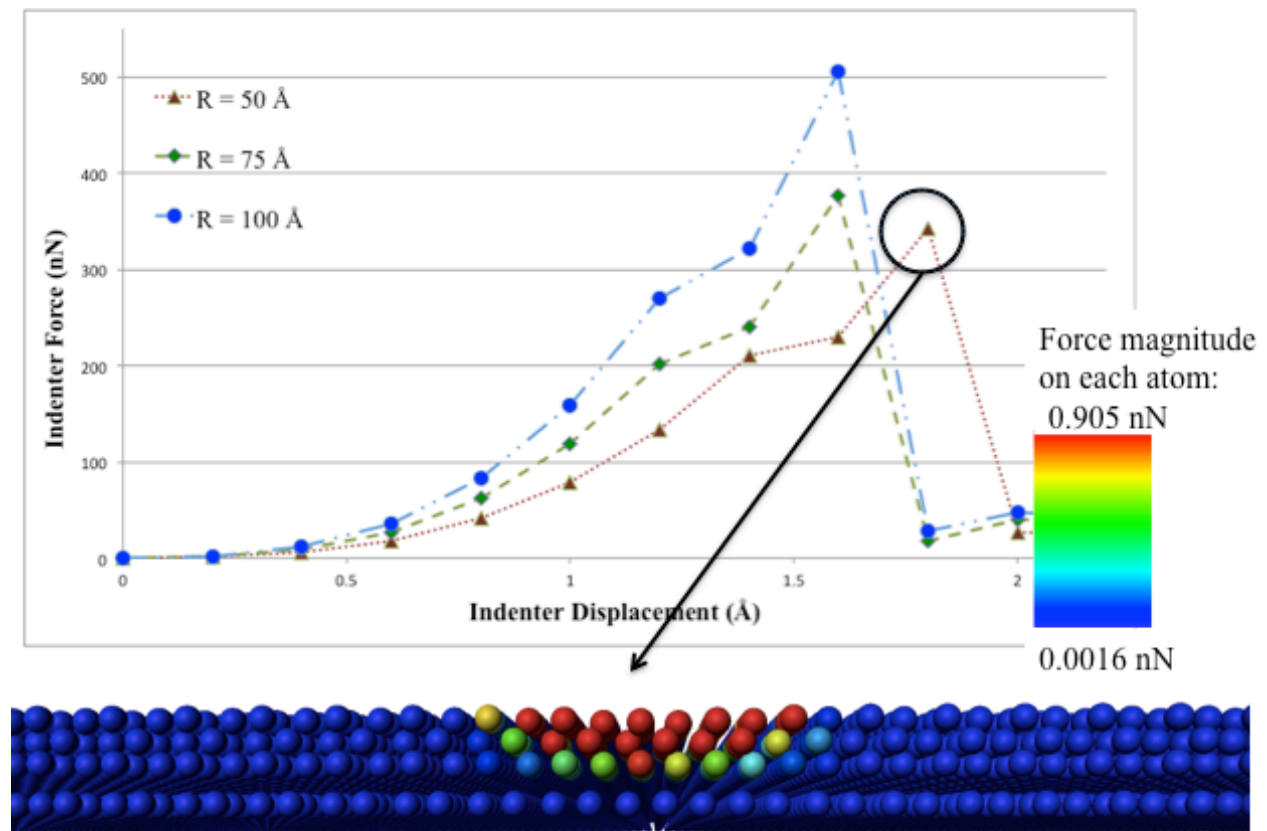
Figure 4.6: Atomic configurations and atomic force magnitudes for the 50 Å nanoindentation simulation before the indenter force drop shown in the force - displacement curve.
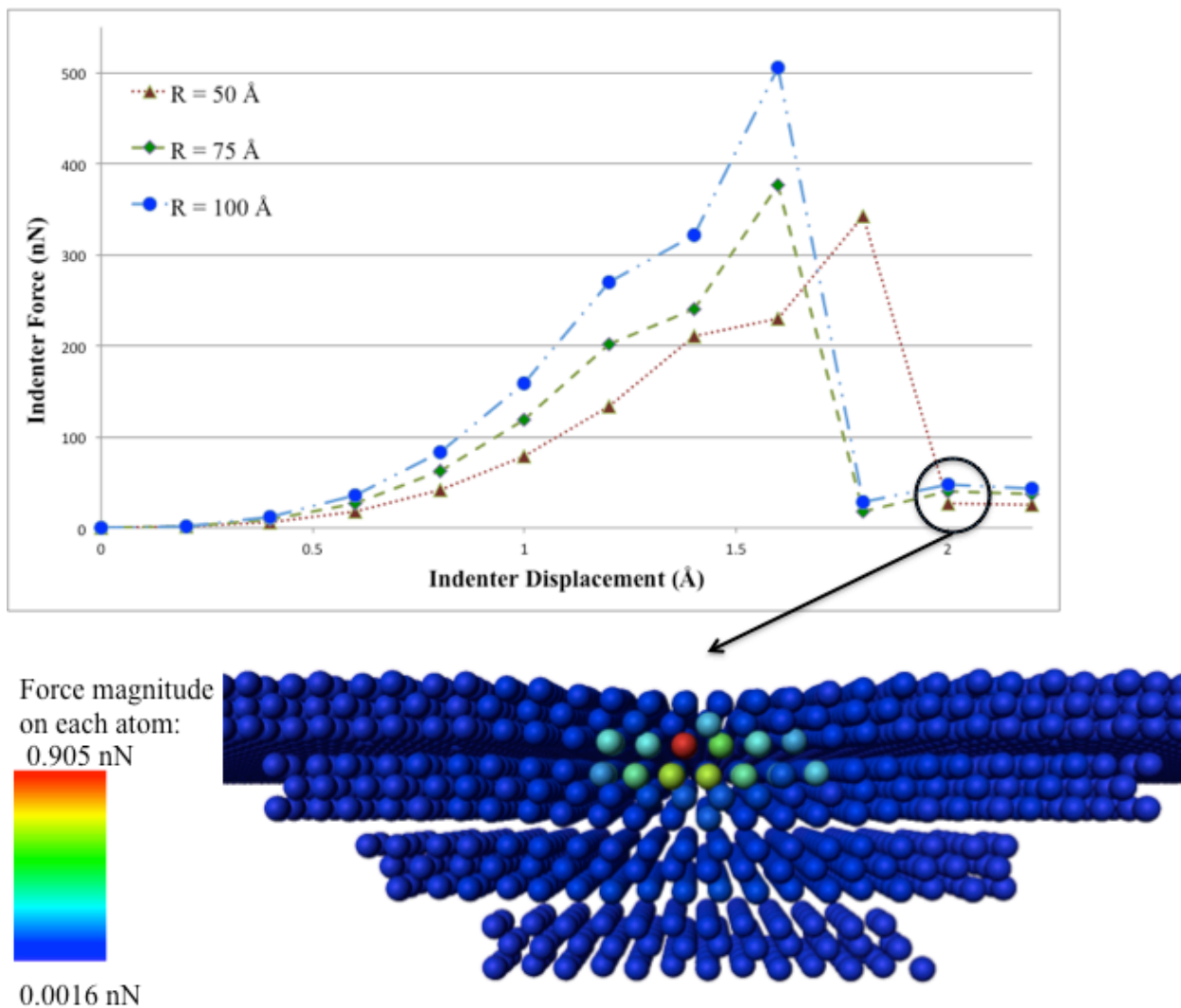
Figure 4.7: Atomic configurations and atomic force magnitudes for the 50 Å nanoindentation simulation after the indenter force drop shown in the force - displacement curve.

With it shown that these initial sudden force drop events corresponded to energetically stable plastic deformation of the MoS_2 crystal, it was necessary to determine the mechanism associated with these plastic events. As mentioned in Section 1.3, the hypothesized deformation mechanism was proposed to be the occurrence of broken bonds. As such, the approach taken in this work was to explicitly analyze the atomic bonding between atoms before and after the sudden force drop event (elastic to plastic transition). This was done to specifically determine if

the sudden drop in the indenter force was due to the breaking of atomic bonds within a MoS_2 tri-layer. To do this analysis, a MATLAB script was written that would compare the atomic bonding distance between all pairs of atoms in the system. If a pair of atoms that was considered a bonded pair of atoms before the plastic event had increased in atomic separation to a distance outside the maximum cutoff defined by the REBO potential, then those atoms were considered to have broken bonds. Surprisingly, in analyzing the bonding of atoms before and after the plastic events, it was observed that no broken bonds occurred during the first force drop event (plastic deformation event). However, as the indenter is displaced further into the MoS_2 crystal, broken bond were observed to occur at depths of 7.8 Å for the 50 Å indenter and 8.6 Å for the 75 Å indenter. There were no broken bonds observed for the 100 Å indenter with a 10 Å nanoindentation depth. Therefore, it has been shown that the primary deformation mechanism associated with the initial indenter force drop event is not a result of broken bonds. As such, another deformation mechanism must occur for this sudden force drop to occur and be energetically stable and permanent. Using OVITO [85] to visualize these deformation events, other possible mechanisms were identified as (i) a relative slip between sulfur atoms within neighboring MoS_2 layers and (ii) a local phase transformation where the atoms or layers move into another related MoS_2 structure that is energetically stable.

To initiate a study of possible relative slip between sulfur atoms between MoS_2 tri-layers, a slip vector analysis [70] was used. Zimmerman *et al*. [70] developed the slip vector to identify a dislocations Burgers vector due to nanoindentation. Using the slip vector it is possible to differentiate elastic and plastic strains [70, 74]. The slip vector is defined as the relative displacement of atoms from their neighbors in an initial configuration to some current configuration during a simulation [70, 74] and is given by the following expression [70]:

$$\mathbf{S}^\alpha = -\frac{1}{n_s} \sum_{\beta \neq \alpha} \left(\mathbf{x}^{\alpha\beta} - \mathbf{X}^{\alpha\beta} \right)$$

Equation 4.5

In Equation 4.5, β are the atomic neighbors to atom α, n_s is the total number of slipped neighbors, $\mathbf{x}^{\alpha\beta}$ is the vector difference between atoms α and β in the initial atomic configuration and $\mathbf{X}^{\alpha\beta}$ is the vector difference between atoms α and β in a current configuration.

To perform the slip vector analysis, a MATLAB script was written to compare the atomic configurations of the MoS_2 system before plastic deformation (maximum indenter force), after plastic deformation and with the indenter fully retracted to its initial position before nanoindentation occurred. Figure 4.8 shows the atomic configurations for these three indenter displacements for the 50 Å indenter. In Figure 4.8, the top image shows that slip only occurs in the sulfur atoms directly below the indenter. The middle image shows that there is a ring of relatively large slip that occurs off the indenter axis, while the atoms directly under the indenter return to a less slipped state. In the bottom image of Figure 4.8, the indenter is fully retracted from the MoS_2 crystal. However, as shown in this image, there is permanent slip left in the lattice. Therefore, this slip vector analysis has shown, in agreement with the force - displacement curves, that there is permanent deformation (slip) of the MoS_2 lattice due to nanoindentation that is energetically stable.
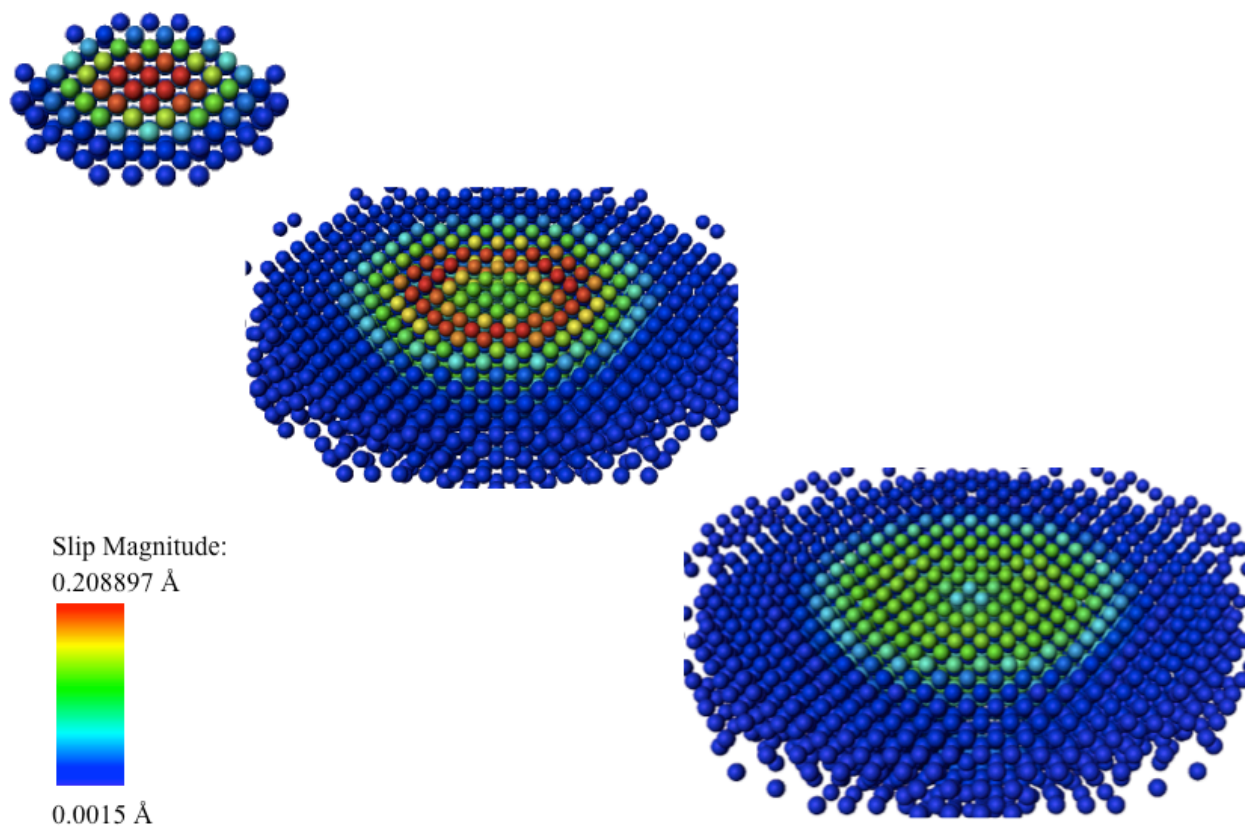
Figure 4.8: **Top**: Atomic configuration before sudden force drop, **Middle**: Atomic configuration after sudden force drop, **Bottom**: Atomic configuration with fully retracted indenter. Atoms are colored according to their relative slip magnitude.

4.4   Summary

In summary, nanoindentation simulations of crystalline MoS_2 were performed with three different indenter sizes to study the elastic response of MoS_2 and the mechanism associated with plastic deformation. In these simulations, it was found that MoS_2 did not follow the Hertzian prediction of a materials elastic response. This was attributed to the fact that MoS_2 is not isotropic but rather highly anisotropic due to its layered structure. In investigating the plastic deformation events due to nanoindentation, it was found that three large and sudden drops in the indenter force occurred, which correspond to plastic deformation events. It was observed that

broken bonds were not the main mechanism associated with the first plastic deformation event contrary to the initial hypothesis. However, broken bonds were observed for two of the three indenters as they were displaced to a depth of 10 Å. From the force - displacement curves and the slip vector analysis, it was shown that there is permanent deformation that occurs due to nanoindentation and permanent slip between atoms even when the indenter is fully retracted that is energetically stable. From the force - displacement curves, the slip vector analysis and using OVITO possible deformation mechanisms identified for further study are (i) relative slip between sulfur atoms in neighboring MoS_2 layers and (ii) a local phase transformation to an energetically stable structure.

CHAPTER 5:   CONCLUSION

5.1   Summary of Work

In this work, a reactive empirical bond-order (REBO) potential that has been parameterized for Mo-S systems and specifically to study the tribological properties of MoS_2 has been successfully programmed into the LAMMPS (Large-scale Atomic Molecular Massively Parallel Simulator) classical atomistic simulation package. It was verified and shown that the LAMMPS implementation of this Mo-S REBO potential is consistent with the energy and force expressions associated with the REBO potential as well as the Liang *et al*. [28] atomistic code. Using this newly implemented LAMMPS potential, the lattice and elastic constants of BCC molybdenum and MoS_2 were calculated and shown to be consistent with the Liang *et al*. [28] atomistic code results as well as experimental [28] and density functional theory [34] results. To achieve this consistency, a new parameter, ε, for the S-S Lennard-Jones interactions was chosen to better reproduce the C_{33} elastic constant of MoS_2 for molecular statics calculations. As such, the LAMMPS implementation of the Mo-S REBO potential accurately described the structural and mechanical properties of MoS_2.

In addition to implementing this Mo-S potential into LAMMPS, this Mo-S potential was used to investigate defect nucleation via nanoindentation simulations with a spherical indenter using LAMMPS. Nanoindentation simulations were carried out on the basal plane of crystalline MoS_2 with three different sized indenters. From these nanoindentation simulations, it was shown that MoS_2 does not follow the Hertzian theory of contact deformation due to its layered structure and highly anisotropic behavior. It was also shown from these simulations, using the force - displacement curves and slip vector analysis that the first sudden indenter force drop does

correspond to permanent plastic deformation with permanent slip occurring. It was shown, by explicit bond distance analysis, that the breaking of atomic bonds is not the main mechanism associated with the initial plastic deformation event of MoS_2. From the visualization of the nanoindentation simulations it was hypothesized that other possible deformation mechanisms are (i) a relative slip between sulfur atoms and (ii) a local phase transformation to a related and energetically stable MoS_2 structure. Additional investigations into the relative slip of interlayer atoms and the local phase transformation of the MoS_2 crystal will need to be performed to determine the precise deformation mechanism due to nanoindentation.

5.2   Recommendations for Future Work

The main focus of this work was the nucleation of defects in an infinite MoS_2 crystal. To gain a more thorough understanding of how MoS_2 nanoparticles may be tuned for use in different lubricating conditions, it will be necessary to study defect nucleation in MoS_2 nanoparticles of varying sizes. This can be accomplished by nanoindentation simulations of MoS_2 crystals of different sizes with free surfaces.

Since the main focus of this work was the nucleation of defects via nanoindentation, no simulations were carried out on the effects of defects on the interlayer frictional properties of MoS_2. As such, to understand how these defects alter the frictional properties of MoS_2 it is necessary to investigate how existing defects migrate within a MoS_2 crystal and how the mobility of the defect can change the interlayer sliding of MoS_2 layers. The effects of these defects can be studied via nanoindentation or by application of a shearing force to the MoS_2 crystal with a defect introduced into the system beforehand.

The proposed use of MoS_2 is to have it intercalated with organic molecules to provide better boundary lubrication performance. However, it is unknown how intercalated organic molecules alter the nanostructure of MoS_2 nanoparticles. Therefore, it is necessary to understand how the organic molecules interact with MoS_2 and what role the organic molecules have on the nanoparticle structure and the interlayer interactions. Also, since the main lubricating property of MoS_2 is exfoliation of the tri-layers, it is necessary to study how the intercalated molecules affect the exfoliation of the tri-layers as well as the frictional sliding of the tri-layers during mechanical deformation and shearing.

Recently it has been discovered that grain boundaries exist in MoS_2 nanoparticles [89]. The presence and movement of grain boundaries can affect the structural and mechanical properties of materials such as: deformation ability, elasticity, and plasticity. The presence of grain boundaries may therefore alter the way MoS_2 nanoparticles perform in lubricating situations. As such, it will be necessary to study how the presence of grain boundaries alters the mechanical and tribological performance of MoS_2 nanoparticles in pure MoS_2 and MoS_2 intercalated with organic molecules via nanoindentation and shearing simulations.

REFERENCES

1.	Persson, B.N.J. (1994). Theory of friction: The role of elasticity in boundary lubrication. Physical Review B, **50**, 4771-4786.

2.	Zilberman, S., Persson, B.N.J., Nitzan, A., Mugele, F., and Salmeron, M. (2001). Boundary lubrication: Dynamics of squeeze-out. Physical Review E, **63**, 055103 (1-4).

3.	Bakunin, V.A., Suslov, A. Yu., Kuzmina, G.N., and Parenago, O.P. (2004). Synthesis and application of inorganic nanoparticles and lubricant components – a review. Journal of Nanoparticle Research, **6**, 273-284.

4.	Kovalev, E.P., Ignatiev, M.B., Semenov, A.P., Smirnov, N.I., Nevolin, V.N., and Fominskii, V. Yu. (2004). Solid Lubricating Coatings for Machines and Mechanisms operating Under Extreme Conditions (A Review). Journal of Friction and Wear, **25**, 78-94.

5.	Malshe, A.P. and Spearot, D.E. (2010). Fundamental Understanding of Nanoparticle-Based Lubricants Tuned to Respond to Harsh Boundary Lubrication Conditions. National Science Foundation (NSF) Grant Proposal.

6.	Watanabe, S. Noshiro, J. and Miyake, S. (2004). Tribological characteristics of WS_2/MoS_2 solid lubricating multilayer films. Surface & Coatings Technology, **183**, 347-351.

7.	Erdemir, A. (2005). Review of engineered tribological interfaces for improved boundary lubrication. Tribology International, **38**, 249-256.

8.	Jost, P.H. (2011). Tribology Micro & Macro Economics: A Road to Economic Savings. Tribology and Lubrication Technology, **61,** 18-22.

9.	Hsu, S.M. and Gates, R.S. (2005). Boundary lubricating films: formation and lubrication mechanism. Tribology International, **38**, 305-312.

10.	Matveevskii, R.M. (1995). Problems of boundary lubrication. Tribology International, **28**, 51-54.

11.	Bartz, W.J. (1978). Tribology, Lubricants and Lubrication Engineering – A Review. Wear, **49**, 1-18.

12.	Maru, M.M. and Tanaka, D.K. (2007). Consideration of Stribeck Diagram Parameters in the Investigation on Wear and Friction Behavior in Lubricated Sliding. Journal of the Brazilian Society of Mechanical Science and Engineering, **XXIX**, 55-62.

13.   Hironaka, S. (1984). Boundary Lubrication and Lubricants. Three Bond Technical News, **9**, 1-8.

14.   Surface Science and Technology. Oct 2011. Department of Materials at the ETH Zurich. Retrieved 27 February 27th, 2012. <http://www.surface.mat.ethz.ch/education/ courses/surfaces_and_interfaces >

15.   Bhushan, B., Israelachvill, J.N., and Landman, U. (1995). Nanotribology: friction, wear and lubrication at the atomic scale. Nature, **374**, 607-616.

16.   Xu, J., Zhu, M.H., Zhou, Z.R., Kapsa, P., and Vincent, L. (2003). An investigation on fretting wear life of bonded MoS_2 solid lubricant coatings in complex conditions. Wear, **255**, 253-258.

17.   Farr, J.P.G. (1975). Molybdenum Disulphide in Lubrication, A Review. Wear, **35**, 1-22.

18.   Stoyanov, P., Fishman, J.Z., Lince, J.R., and Chromik, R.R. (2008). Micro-tribological performance of MoS_2 lubricants with varying Au content. Surface & Coatings Technology, **203**, 761-765.

19.   Arbabi, H. and Eyre, T.S. (1986). Investigation into the lubricating effectiveness of molybdenum disulphide dispersion in a fully formulated oil. Tribology International, **19**, 87-91.

20.   Hu, X. (2005). On the size effect of molybdenum disulphide particles on the tribological performance. Industrial Lubrication and Tribology, **57**, 255-259.

21.   Thorp, J.M. (1973). The Mechanism of Lubrication by Molybdenum Disulphide Dispersed in Oil and the Effect of a Zinc Dialkyldithiophosphate Additive. Wear, **23**, 63-70.

22.   Antony, J.P., Mittal, B.D., Naithani, K.P., Misra, A.K. and Bhatnagar, A.K. (1994). Anitwear/extreme pressure performance of graphite and molybdenum disulphide combinations in lubricating greases. Wear, **174**, 33-37.

23.   Holinski, R. and Gansheimer, J. (1971). A Study of the Lubricating Mechanism of Molybdenum Disulfide. Wear, **19**, 329-342.

24.   Winer, W.G. (1967). Molybdenum Disulfide as a Lubricant: A Review of the Fundamental Knowledge. Wear, **10**, 422-452.

25.   Martin, J.M., Donnet, C. and Le Monge, Th. (1993). Superlubricity of molybdenum disulphide. Physical Review B, **48**, 10583-10586.

26. Verma, A., Jiang, W., Abu Safe, H.H., Brown, W.D. and Malshe, A.P. (2008). Tribological Behavior of Deagglomerated Active Inorganic Nanoparticles for Advanced Lubrication. Tribology Transactions, **51**, 673-678.

27. Singer, I.L., Bolster, R.N., Wegand, J., Fayeulle, S. and Stupp, B.C. (1990). Hertzian stress contribution to low friction behavior of thin MoS_2 coatings. Applied Physics Letters, **57**, 995-997.

28. Liang, T., Phillpot, S.R. and Sinnott, S.B. (2009). Parameterization of a reactive many-body potential for Mo-S systems. Physical Review B, **79**, 245110 (1-14).

29. Electron Microscopy Unit. Ed. Ronit Popovitz-Biro. May 2011. Weizmann Institute of Science. Retrieved February 27th, 2012. <http://www.weizmann.ac.il/Chemical_ Research_Support /EM_Unit/Ronit/current-activities>

30. US Research Nanomaterials, Inc. Retrieved February 27th, 2012 <http://www.us-nano.com/inc/sdetail/3821>

31. Hoyt, J. (2001). Computational Materials Science: A Powerful and Predictive Tool. Journal of the Minerals, Metals and Materials Society, **53**, 14.

32. Wei, L., Jun-Fang, C., Qinyu, H. and Teng, W. (2010). Electronic and elastic properties of MoS_2. Physica B, **405**, 2498-2502.

33. Chermette, H., Rogemond, F., Beqqali, O.E., Paul, J.F., Donnet, C., Martin, J.M. and Le Mogne, T. (2001). Lubricating properties of molybdenum disulphur: a density functional theory study. Surface Science, **472**, 97-110.

34. Alexiev, A., Prins, R. and Weber, T. (2000). *Ab initio* study of MoS_2 and Li absorbed on the $(10\bar{1}0)$ face of MoS_2. Physical Chemistry Chemical Physics, **2**, 1815-1827.

35. Todorova, T., Alexiev, A., Prins, R. and Weber, T. (2004). Ab *initio* study of 2H-MoS_2 using Hay and Wadt effective core pseudo-potentials for modeling the $(10\bar{1}0)$ surface structure. Physical Chemistry Chemical Physics, **6**, 3023-3030.

36. Stefanov, M., Enyashin, A.N., Heine, T. and Seifert, G. (2008). Nanolubrication: How Do MoS_2-Based Nanostructures Lubricate? Physical Chemistry C, **112**, 17764-17767.

37. Varshney, V., Patnaik, S.S., Muratore, C., Roy, A.K., Voevodin, A.A. and Farmer, B.L. (2010). MD simulations of molybdenum disulphide (MoS_2): Force-field parameterization and thermal transport behavior. Computational Materials Science, **48**, 101-108.

38. Morita, Y., Onodera, T., Suzuki, A., Sahnoun, R., Koyama, M., Tsuboi, H., Hatakeyma, N., Endou, A., Takaba, H., Kubo, M., Del Carpio, C.A., Shin-yoshi, T., Nishino, N., Suzuki, A. and Miyamoto, A. (2008). Development of a new molecular dynamics method

for tribochemical reaction and its application to formation dynamics of MoS_2 tribofilm. Applied Surface Science, **254**, 7618-7621.

39.   Brunier, T.M., Drew, M.G.B. and Mitchell, P.C.H. (1992). Molecular Mechanics Studies of Molybdenum Disulphide Catalysts Parameterisation of Molybdenum and Sulphur. Molecular Simulation, **9**, 143-159.

40.   Brunier, T.M., Drew, M.G.B. and Mitchell, P.C.H. (1992). Molecular Mechanics Study of the Interaction of Thiophene with a Molybdenum Disulfide Catalyst. Journal of the Chemical Society: Faraday Transactions, **88**, 3225-3232.

41.   Abraham, F.F., Walkup, R., Gao, H., Duchaineau, M., De La Rubia, T.D. and Seager, M. (2001). Simulating materials failure by using up to one billion atoms and the world's fastest computer: Work-hardening. Proceedings of the National Academy of Science, **99**, 5783-5787.

42.   Allen, M.P. (2004). Introduction to Molecular Dynamics. Computational Soft Matter: From Synthetic Polymers to Proteins, **23**, 1-28.

43.   Allen M.P. and Tildesley, D.J. (1987). Computer Simulations of Liquids, Clarendon Press, Oxford.

44.   Elliot, S.R. (1998). The Physics and Chemistry of Solids, John Wiley & Sons, Chichester.

45.   Ercolessi, F. (1997). A Molecular Dynamics Primer.

46.   Frenkel, D. and Smit, B. (2002). Understanding Molecular Simulation From Algorithms to Applications, Academic Press, San Diego.

47.   Hernandez, E.R. (2008). Molecular Dynamics: from basic techniques to applications (A Molecular Dynamics Primer). American Institute of Physics, Conf. Proc. 1077, 95-123.

48.   Pathria, R.K. and Beale, P.D. (2011). Statistical Mechanics, Academic Press, Amsterdam.

49.   Plimpton, S. (1995). Fast Parallel Algorithms for Short-Range Molecular Dynamics, Journal of Computational Physics, 117, 1-19. < http://lammps.sandia.gov >.

50.   Bitzek, E. Koskinen, P., Gahler, F., Moseler, M. and Gumbsch, P. (2006). Structural Relaxation Made Simple. Physical Review Letters, **97**, 170201(1-4).

51.   Shewchuk, J.R. (1994). An introduction to the conjugate gradient method without the agonizing pain. Carnegie Mellon University.

52.   Brenner, D.W. (2000). The Art and Science of an Analytic Potential. Physica Status Solidi B, **23**, 23-40.

53.   Carlsson, A.E. (1990). Beyond pair potentials in elemental transition metals and semiconductors. <u>Solid State Physics</u>, 43, Academic Press, New York, 1-91.

54.   Finnis, M. (2004). <u>Interatomic Force in Condensed Matter</u>. Oxford University Press.

55.   Abell, G.C. (1985). Empirical chemical pseudopotential theory of molecular and metallic bonding. Physical Review B, **31**, 6184-6196.

56.   Tersoff, J. (1988). New empirical approach for the structure and energy of covalent systems. Physical Review B, **37**, 6991-7000.

57.   Tersoff, J. (1988). Empirical Interatomic Potential for Carbon, with Applications to Amorphous Carbon. Physical Review Letters, **61**, 2879-2882.

58.   Tersoff, J. (1989). Modeling solid-state chemistry: Interatomic potentials for multicomponent systems. Physical Review B, **39**, 5566-5568.

59.   Brenner, D.W. (2002). A second-generation reactive empirical bond order (REBO) potential energy expression for hydrocarbons. Journal of Physics: Condensed Matter, **14**, 738-802.

60.   Liu, A. and Stuart, S.J. (2007). Empirical Bond-Order Potential for Hydrocarbons: Adaptive Treatment of van der Waals Interactions. Journal of Computational Chemistry, **29**, 601-611.

61.   Tanaka, J., Abrams, C.F. and Graves, D.B. (2000). New C-F interatomic potential for molecular dynamics simulation of fluorocarbon film formation. Journal of Vacuum Science and Technology A, **18**, 938-945.

62.   Que, J.Z., M.W., Radny and Smith, P.V. (2000). Application of the extended Brenner potential to the Si(111) 7x7: H System II: periodic calculations. Surface Science, **444**, 140-155.

63.   Plaisted, T.A., Ni, B., Zahrt, J.D. and Sinnott, S.B. (2000). Comparison of growth of hydrocarbon thin films by molecular-beam and cluster-beam deposition: atomistic simulations. Thin Solid Films, **381**, 73-83.

64.   Ni, B. and Sinnott, S.B. (2001). Tribological properties of carbon nanotube bundles predicted from atomistic simulations. Surface Science, **487**, 87-96.

65.   Zhang, S., Mielke, S.L., Khare, R., Troya, D., Ruoff, R.S., Schatz, G.C. and Belytschko, T. (2005). Mechanics of defects in carbon nanotubes: Atomistic and multiscale simulations. Physical Review B, **71**, 115403(1-12).

66. Jones, J.E. (1924). On the Determination of Molecular Fields. I. From the Variation of the Viscosity of a Gas with Temperature. Proceedings of the Royal Society of London Series A, **106**, 441-462.

67. Jones, J.E. (1924). On the Determination of Molecular Fields. II. From the Equation of State of a Gas. Proceedings of the Royal Society of London Series A, **106**, 463-477.

68. Nair, A.K., Farkas, D. and Kriz, R.D. (2008). Molecular Dynamics Study of Size Effects and Deformation of Thin Films due to Nanoindentation. Computer Modeling in Engineering and Sciences, **24**, 239-248.

69. Szlufarska, I. (2006). Atomistic simulations of nanoindentation. Materials Today, **9**, 42-50.

70. Zimmerman, J.A., Kelchner, C.L., Klein, P.A., Hamilton, J.C. and Foiles S.M. (2001). Surface Step Effects in Nanoindentation. Physical Review Letters, **87**, 165507(1-4).

71. Tsuru, T. and Shibutani, Y. (2007). Anisotropic effects in elastic and incipient plastic deformation under (001), (110), and (111) nanoindentation of Al and Cu. Physical Review B, **75**, 035415(1-6).

72. Kelchner, C.L., Plimpton, S.J. and Hamilton, J.C. (1998). Dislocation nucleation and defect structure during surface indentation. Physical Review B, **58**, 11085-11088.

73. Njiem, E.K. and Bahr, D.F. (2010). Atomistic simulations of nanoindentation in the presence of vacancies. Scripta Materialia, **62**, 598-601.

74. Lilleodden, E.T., Zimmerman, J.A., Foiles, S.M. and Nix, W.D. (2003). Atomistic simulations of elastic deformation and dislocation nucleation during nanoindentation. Journal of the Mechanics and Physics of Solids, **52**, 901-920.

75. Liang, H.Y., Woo, C.H., Huang, H., Ngan, A.H. and Yu, T.X. (2003). Dislocation nucleation in the initial stage during nanoindentation. Philosophical Magazine, **83**, 3609-3622.

76. Wagner, R.J., Ma, L., Tavazza, F. and Levine, L.E. (2008). Dislocation nucleation during nanoindentation of aluminum. Journal of Applied Physics, **104**, 114311(1-4).

77. Szlufarska, I. (2007). A molecular dynamics study of nanoindentation of amorphous silicon carbide. Journal of Applied Physics, **102**, 023509(1-9).

78. Smith, R., Christopher, D., Kenny, S.D., Richter, A. and Wolf, B. (2003). Defect generation and pileup of atoms during nanoindentation of Fe single crystals. Physical Review B, **67**, 245405(1-10).

79.   Dupont, V. and Sansoz, F. (2008). Molecular dynamics study of crystal plasticity during nanoindentation in Ni nanowires. Journal of Materials Research, **24**, 948-956.

80.   Sansoz, F. and Dupont, V. (2010). Nanoindentation and plasticity in nanocrystalline Ni nanowires: A case study in size effect mitigation. Scripta Materialia, **63**, 1136-1139.

81.   Richter, A., Ries, R., Smith, R., Henkel, M. and Wolf, B. (2000). Nanoindentation of diamond, graphite and fullerene films. Diamond and Related Materials, **9**, 170-184.

82.   Boresi, A.P. and Schmidt, R.J. (2003). Advanced Mechanics of Materials. John Wiley & Sons, Inc.

83.   Hertz, H. (1896). Miscellaneous Papers. London: Macmillan, New York, Macmillan and Co. < http://archive.org/details/cu31924012500306>.

84.   Callister, W.D., (2003). Materials Science and Engineering An Introduction. John Wiley & Sons, Inc.

85.   Stukowski, A. (2010). Visualization and analysis of atomistic simulation data with OVITO – the Open Visualization Tool. Modelling and Simulation in Materials Science and Engineering, **18**, 015012.

86.   Lin, Y.H. and Chen, C.H. (2008). A molecular dynamics study of phase transformations in mono-crystalline Si under nanoindentation. Applied Physics A: Materials Science & Processing, **92**, 571-578.

87.   CSM Instruments. Nanoindentation with spherical indenters for characterization of stress-strain properties. < http://www.csm-instruments.com/Nanoindentation-with-spherical-indenters-for-characterization-of-stress-strain-properties >

88.   Bushby, A.J. and Dunstan, D.J. (2004). Plasticity size effects in nanoindentation. Journal of Materials Research, **19**, 137-142.

89.   Private communications with Dr. Ajay Malshe and Dr. Douglas Spearot. (Spring Semester 2011)

Appendix A: Description of Research for Popular Publication

Better Lubrication with Supercomputers

By: James Stewart

Friction is a part of everyday life. Friction prevents cars from sliding off of the road and helps keep you standing upright when walking. It is very useful and needed in life but it also has its disadvantages in that it can cause mechanical components such as engine pistons to wear at faster rates than desired and cause a reduction in efficiency. At the University of Arkansas, James Stewart, a M.S. student in the interdisciplinary Microelectronics-Photonics graduate program, is working under Dr. Douglas Spearot to investigate ways to reduce this friction.

Surfaces of mechanical components that slide against each other during operation are not flat, containing rough patches called asperities. As the surfaces slide against each other, the asperities collide and hinder the movement of the components. This process causes mechanical components to wear down and become dangerous or impractical for continued use. Therefore, lubrication is applied to these components to prevent these asperities to come into contact.

However, Mr. Stewart says, "There are two problems with traditional lubricants used at high temperatures and pressures. First, as the temperature and pressure increase, the lubricant could break down or even rupture. Thus, the lubricant would no longer provide a low friction barrier between components and the asperities would start colliding. Second, if the asperities are to small, the additives in the lubricant, which are normally micron sized, will not be able to navigate the surface of the components and properly cover the asperities."

As such, it is important to develop a nanoparticle-additive-based lubricant that can work at high temperatures and pressures and at the same time navigate the surface asperities. Dr. Spearot and his collaborators at the University of Arkansas have proposed Molybdenum

disulphide (MoS$_2$) nanoparticles integrated with organic fatty acids as a possible solution to these problems. While experimental studies have shown that this novel nanoparticle based lubricant does provide desired lubricating properties, the studies are not able to examine how these nanoparticles deform under mechanical contact, which the nanoparticles experience during synthesis and application.

Mr. Stewart continued, "To be able to design these nanoparticle additives to work in specific temperature and pressure regimes, it is necessary to understand how defects nucleate in these nanoparticles." To achieve this, Dr. Spearot's group is employing atomistic simulations.

Atomistic simulations model materials at the atomic level and can therefore capture the fundamental mechanisms associated with failure. Using visualization software, it is possible to observe the formation of defects in MoS$_2$ nanoparticles during an applied load such as nanoindentation as shown in Figure 1.
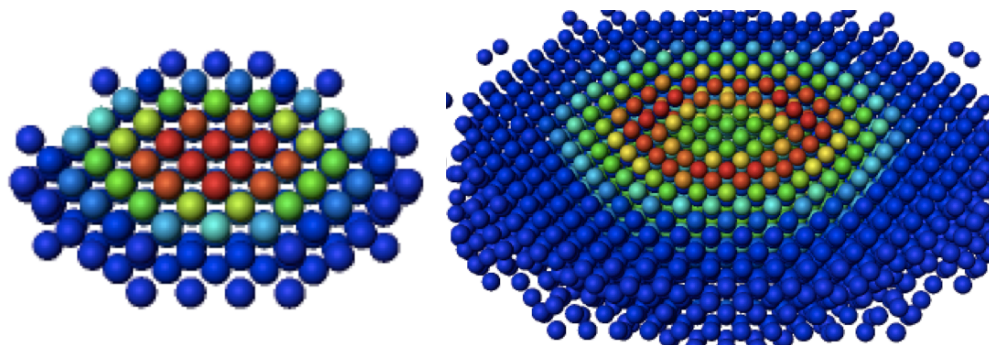
Figure 1: Atomic configurations (colored by atomic force magnitude) of thin film MoS$_2$ before and after failure due to nanoindentation. Images were created and provided by Mr. Stewart using OVITO.

Mr. Stewart noted, "In using atomistic simulations, it is easy to change environmental conditions such as the temperature and pressure or even the size of the nanoparticles and observe the behavior of the nanoparticles." Therefore, atomistic simulations allow for an insight into the

fundamental mechanisms of deformation in the nanoparticles at different environmental conditions that are characteristic of the synthesis and application of the nanoparticles that cannot be captured experimentally.

This information will allow for the researchers at the University of Arkansas to control the synthesis parameters to tune the frictional properties of the nanoparticles to specific temperature and pressure regimes and in turn provide better lubrication to everyday mechanical components.

Figure 2: Picture of the Arkansas High Performance Computing Center used by Dr. Spearot and his group along with other researchers at the University of Arkansas.

Appendix B: Executive Summary of Newly Created Intellectual Property

The following list of new intellectual property items were created in the course of this work and should be considered from both a patent and commercialization perspective.

1. A C++ code to compute a reactive empirical bond-order (REBO) potential that has been parameterized for Mo-S systems (specifically tribological properties of MoS_2) to be used and distributed with the LAMMPS simulation package.

2. A MATLAB script to use a given neighbor list and atomic position data to determine the separation distance of nearest bonded neighbors and determine if these distances correspond to broken bonds during failure.

3. A MATLAB script to use a given neighbor list and atomic position data to determine a triplet of atoms and the angles corresponding to this atom triplet to determine if a redistribution of angles occurs during failure.

4. A MATLAB script to perform a slip vector analysis using atomic position data output at each indentation depth.

Appendix C: Potential Patent and Commercialization Aspects of Listed IP Items

C1:   Patentability of Intellectual Property

1. The C++ code designed to be used with the LAMMPS simulation package is not patentable because it is part of an open source license.

2. The MATLAB script to determine the occurrence of broken bonds during the nanoindentation simulation is not patentable because the idea is not new. However no open source code was available and an in house code was produced.

3. The MATLAB script to determine the redistribution of angle interactions during the nanoindentation simulation is not patentable because the idea is not new. However no open source code was available and an in house code was produced.

4. The MATLAB script to perform a slip vector analysis from the atomic position data from the nanoindentation simulation is not patentable because the idea is not new. However no open source code was available and an in house code was produced.

C2:   Commercialization Prospects

The implemented version of the Mo-S REBO potential will be submitted to the developers of LAMMPS at Sandia National Labs / Albuquerque, NM to be incorporated into the open-source distribution of LAMMPS.

C3:   Possible Prior Disclosure of IP

Information regarding the implemented version of this potential into LAMMPS was disclosed to the MicroEP community during Research Communications Seminar in the spring 2011 semester as well as Dr. Susan Sinnott's research group at the University of Florida during the potential validation procedure. The MATLAB scripts were disclosed in private meetings with Dr. Spearot.

Appendix D: Broader Impact of Research

D1: **Applicability of Research Methods to Other Problems**

The main idea of simulating nanoindentation of MoS_2 was to determine how defects form and deformation occurs to design nanoparticles for certain uses. It is possible to use nanoindentation (and in fact has been used) to study how a variety of materials generate defects during an applied load. It may also be possible to investigate the generation of broken bonds in defect nucleation in addition to traditional defect and dislocation analysis tools.

D2: **Impact of Research Results on U.S. and Global Economy**

The presented research has the potential to benefit and advance nanoparticle based lubricants by allowing the lubricating properties of the nanoparticles to be controlled during synthesis (tunable nanoparticles). This would allow for an increased reduction in the wear of mechanical components and the excess energy consumed by these machines; therefore decreasing the amount of money spent on these issues.

D3: **Impact of Research Results on Environment**

The creation of tunable nanoparticle based lubricants would allow for improved energy efficiency in machines and components requiring lubrication. Since MoS_2 is environmentally friendly and unreactive, there is no foreseeable harm to the environment with the use of this material.

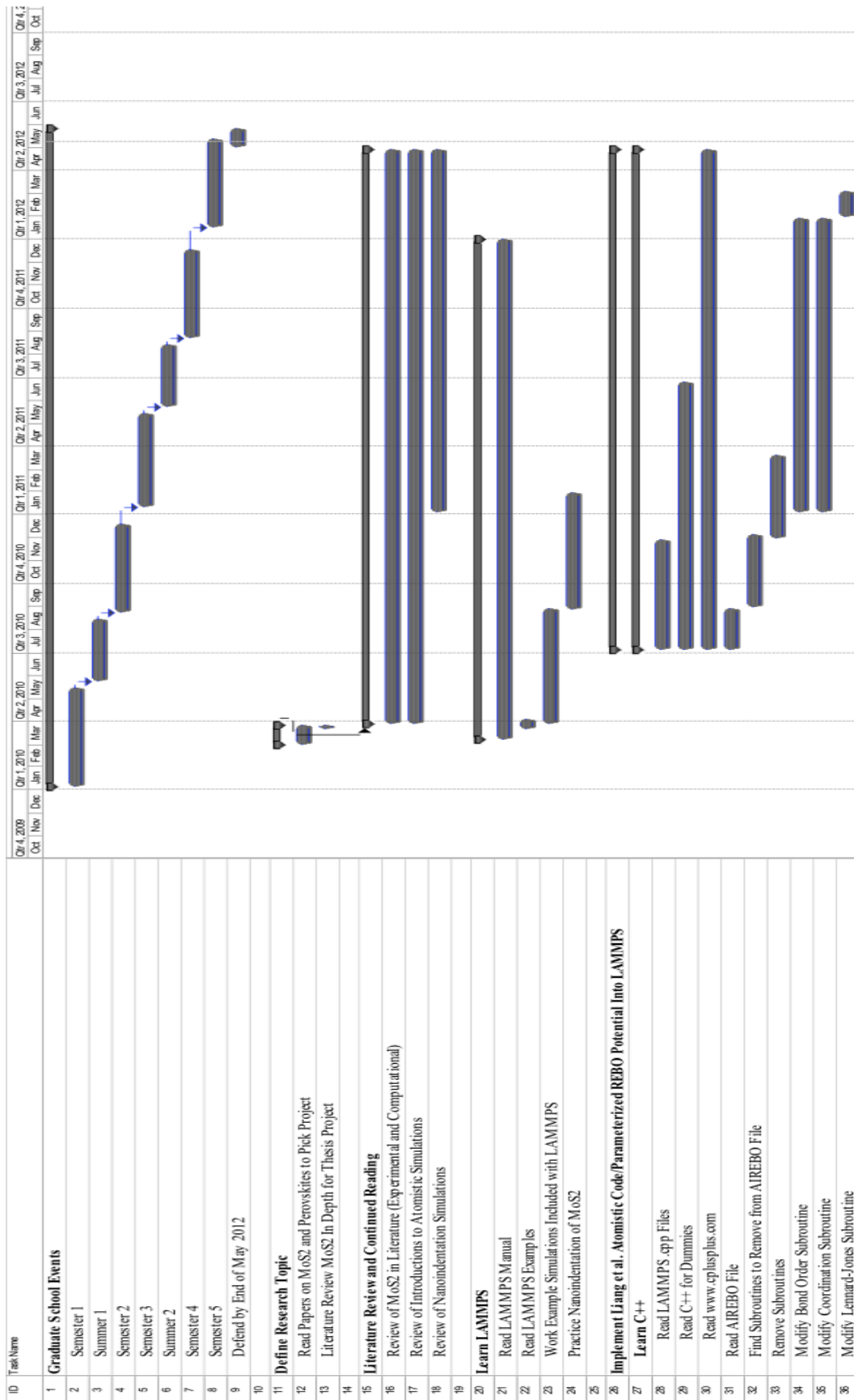**Appendix E: Microsoft Project for MS MicroEP Degree Plan**

ID	Task Name
1	**Graduate School Events**
2	Semester 1
3	Summer 1
4	Semester 2
5	Semester 3
6	Summer 2
7	Semester 4
8	Semester 5
9	Defend by End of May 2012
10	
11	**Define Research Topic**
12	Read Papers on MoS2 and Perovskites to Pick Project
13	Literature Review MoS2 In Depth for Thesis Project
14	
15	**Literature Review and Continued Reading**
16	Review of MoS2 in Literature (Experimental and Computational)
17	Review of Introductions to Atomistic Simulations
18	Review of Nanoindentation Simulations
19	
20	**Learn LAMMPS**
21	Read LAMMPS Manual
22	Read LAMMPS Examples
23	Work Example Simulations Included with LAMMPS
24	Practice Nanoindentation of MoS2
25	
26	**Implement Liang et al. Atomistic Code/Parameterized REBO Potential Into LAMMPS**
27	**Learn C++**
28	Read LAMMPS .cpp Files
29	Read C++ for Dummies
30	Read www.cplusplus.com
31	Read AIREBO File
32	Find Subroutines to Remove from AIREBO File
33	Remove Subroutines
34	Modify Bond Order Subroutine
35	Modify Coordination Subroutine
36	Modify Lennard-Jones Subroutine

Figure E.1: Microsoft Project File for MicroEP M.S. Degree

ID	Task Name
37	
38	**Validate Implemented LAMMPS REBO Code**
39	**3-Atom Known Mo-Mo-Mo Structure**
40	**Calculate Energy Per Atom with LAMMPS and Liang et al. Code**
41	Compare Componentes of Energy Expression (VA, VR, bij, etc.)
42	**Calculate Force Componentes Per Atom with LAMMPS and Liang et al. Code**
43	Compare Componentes of Energy Expression (derivatives of energy components)
44	**3-Atom Known S-S-S Structure**
45	**Calculate Energy Per Atom with LAMMPS and Liang et al. Code**
46	Compare Componentes of Energy Expression (VA, VR, bij, etc.)
47	**Calculate Force Componentes Per Atom with LAMMPS and Liang et al. Code**
48	Compare Componentes of Energy Expression (derivatives of energy components)
49	**3-Atom Known S-Mo-S Structure**
50	**Calculate Energy Per Atom with LAMMPS and Liang et al. Code**
51	Compare Componentes of Energy Expression (VA, VR, bij, etc.)
52	**Calculate Force Componentes Per Atom with LAMMPS and Liang et al. Code**
53	Compare Componentes of Energy Expression (derivatives of energy components)
54	
55	**Test Implemented LAMMPS Code on BCC Molybdenum and Crystalline MoS2**
56	Run BCC Molybdenum Structural Calculations
57	Run BCC Elastic Constants Calculations
58	Run MoS2 Structural Calculations
59	Run MoS2 Elastic Constants Calculations
60	
61	**Data Acquisition**
62	Run 25 Angstrom Radius Indentation
63	Run 40 Angstrom Radius Indentation
64	Run 50 Angstrom Radius Indentation
65	Run 60 Angstrom Radius Indentation
66	Run 75 Angstrom Radius Indentation
67	Run 90 Angstrom Radius Indentation
68	Run 100 Angstrom Radius Indentation
69	Run 115 Angstrom Radius Indentation
70	Run 125 Angstrom Radius Indentation
71	Run 150 Angstrom Radius Indentation
72	Run 175 Angstrom Radius Indentation

Figure E.1: Microsoft Project File for MicroEP M.S. Degree
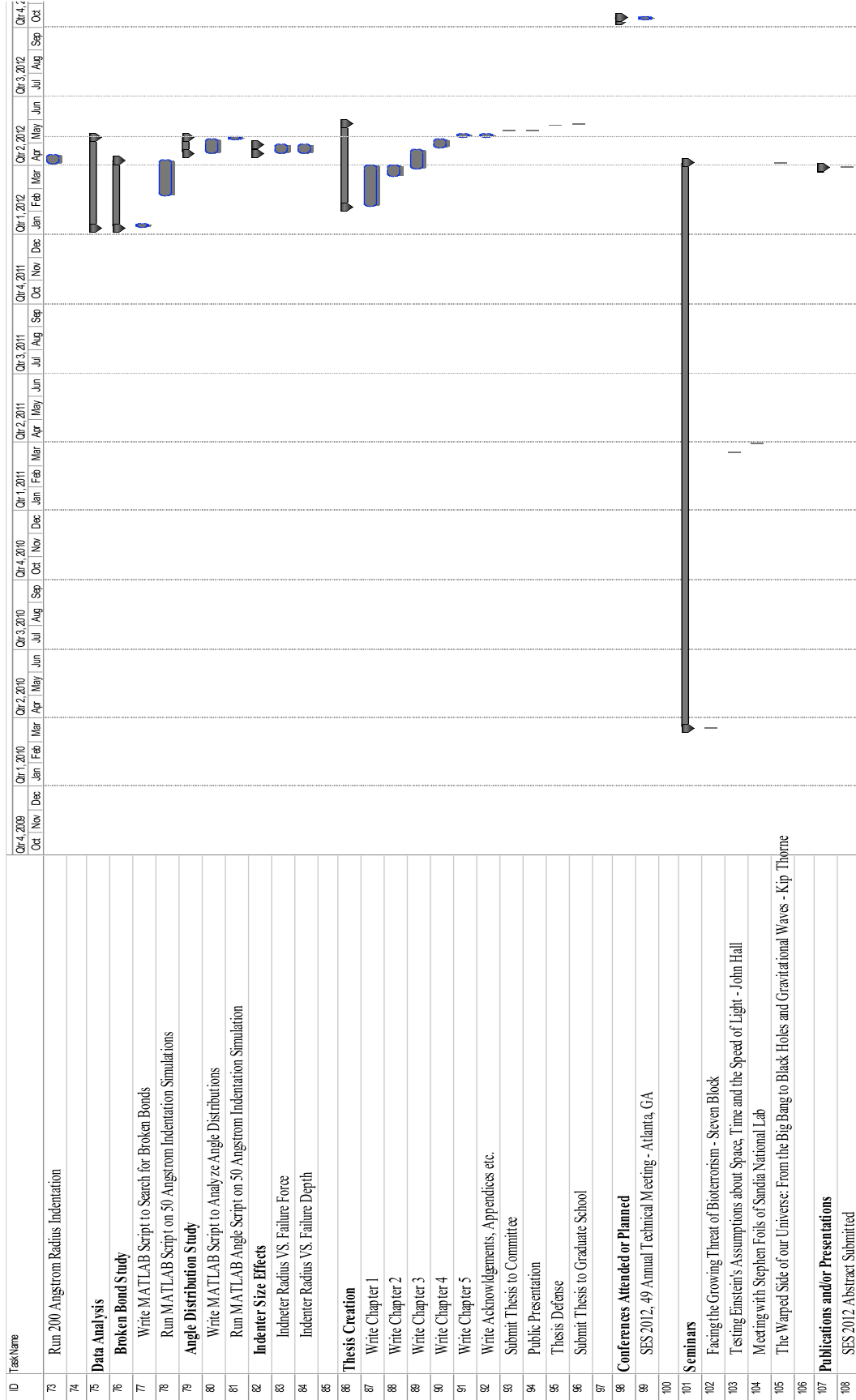
Figure E.1: Microsoft Project File for MicroEP M.S. Degree

Appendix F: Identification of All Software Used in Research and Thesis

Computer #1:
       Model Number: Dell Precision T3500
       Serial Number: 6772145113
       Location: NANO Building Room 213b
       Owner: University of Arkansas (Dr. Douglas Spearot)
       Software #1:
              Name: Microsoft Office 2010
              Purchased by: University of Arkansas Site License
       Software #2:
               Name: MATLAB R2011b
              Purchased by: University of Arkansas Site License
       Software #3:
               Name: Microsoft Project 2007
              Purchased by: University of Arkansas Site License (MicroEP Program)
       Software #4:
               Name: OVITO
              Purchased by: Open Source

Computer #2:
       Model Number: Arkansas High Performance Computing Center
       Location: University of Arkansas
       Owner: University of Arkansas
       Software #1:
               Name: LAMMPS
              Purchased by: Open Source

Computer #3:
       Model Number: Apple EMC 2389
       Serial Number: YD11800JDAS
       Location: Personal Computer
       Owner: James A. Stewart Jr.
       Software #1:
               Name: Microsoft Office for Mac 2011
              Purchased by: James A. Stewart Jr.
       Software #2:
               Name: Apple iWork
              Purchased by: James A. Stewart Jr.

Appendix G: All Publications Published, Submitted and Planned

Submission of the work presented in this thesis on the defect and deformation processes in MoS$_2$ during nanoindentation simulations is planned for the summer and fall of 2012 in either Acta Materialia or Modelling and Simulation in Materials Science and Engineering

Appendix H: Force Expressions for the REBO and Lennard-Jones Potentials

Lennard-Jones Forces:

$$F_{ij}^{LJ}(r_{ij}) = \frac{24\varepsilon}{r_{ij}}\left[2\left(\frac{\sigma_{ij}}{r_{ij}}\right)^{12} - \left(\frac{\sigma_{ij}}{r_{ij}}\right)^{6}\right]$$

Lennard-Jones Spline Forces:

$$F_{ij}^{S-LJ}(r_{ij}) = \frac{(r_{ij} - R_{ij}^{min})}{(0.95\sigma_{ij} - R_{ij}^{min})}\left\{3(r_{ij} - R_{ij}^{min})\left[\frac{-2E_{LJ}(0.95\sigma_{ij})}{(0.95\sigma_{ij} - R_{ij}^{min})^{2}} + \frac{\partial E_{LJ}(0.95\sigma_{ij})}{(0.95\sigma_{ij} - R_{ij}^{min})}\right]\right.$$
$$\left. + 2\left(\frac{3E_{LJ}(0.95\sigma_{ij})}{(0.95\sigma_{ij} - R_{ij}^{min})} - \partial E_{LJ}(0.95\sigma_{ij})\right)\right\}$$

REBO Forces:

$$F_{ij}^{REBO}(r_{ij}) = \sum_{i<j}\left\{\frac{-\partial f_{ij}^{c}(r_{ij})}{\partial r}\left(\left(1 + \frac{Q_{ij}}{r_{ij}}\right)A_{ij}e^{-\alpha_{ij}r_{ij}} - b_{ij}B_{ij}e^{-\beta_{ij}r_{ij}}\right)\right.$$
$$- f_{ij}^{c}(r_{ij})\left(-\left(\alpha_{ij} + \frac{\alpha_{ij}Q_{ij}}{r_{ij}} + \frac{Q_{ij}^{2}}{r_{ij}^{2}}\right)A_{ij}e^{-\alpha_{ij}r_{ij}} + b_{ij}B_{ij}\beta_{ij}e^{-\beta_{ij}r_{ij}}\right)$$
$$\left. + f_{ij}^{c}(r_{ij})B_{ij}e^{-\beta_{ij}r_{ij}}\frac{\partial b_{ij}}{\partial r_{ij}}\right\}$$

where:

$$\frac{\partial b_{ij}}{\partial r_{ij}} = -\frac{1}{2}b_{ij}^{3}\left\{\sum_{k\neq i,j}\left[\frac{\partial f_{ik}^{c}(r_{ik})}{\partial r}G[\cos(\theta_{ijk})] + f_{ik}^{c}(r_{ik})\frac{\partial[\cos(\theta_{ijk})]}{\partial \cos(\theta_{ijk})}\frac{\partial \cos(\theta_{ijk})}{\partial r}\right] + \frac{\partial P}{\partial N_{i}}\frac{\partial N_{i}}{\partial r}\right\}$$

where:

$$\frac{\partial N_{i}}{\partial r_{ij}} = \sum_{k\neq i}\frac{\partial f_{ik}^{c}(r_{ik})}{\partial r}$$

and using the Dot Product:

$$\frac{\partial \cos(\theta_{ijk})}{\partial r} = \frac{\frac{\partial \boldsymbol{r}_{ij}}{\partial r} \cdot \boldsymbol{r}_{ik} + \boldsymbol{r}_{ij} \cdot \frac{\partial \boldsymbol{r}_{ik}}{\partial r}}{|r_{ij}||r_{ik}|} - \frac{\cos(\theta_{ijk})}{|r_{ij}||r_{ik}|} \left(\frac{\partial |r_{ij}|}{\partial r} |r_{ik}| + |r_{ij}| \frac{\partial |r_{ij}|}{\partial r} \right)$$